JOURNAL OF PETROLOGY | VOLUME 55 | NUMBER 8 | PAGES 1595–1617 | 2014 | doi:10.1093/petrology/egu035

Contact Metamorphism of Precambrian Gneiss by the Skaergaard Intrusion

N. AARON BUFE[1]*, MARIAN B. HOLNESS[2] AND MADELEINE C. S. HUMPHREYS[3†]

[1]DEPARTMENT OF EARTH SCIENCES, UNIVERSITY OF CALIFORNIA, SANTA BARBARA, CA 93106, USA
[2]DEPARTMENT OF EARTH SCIENCES, UNIVERSITY OF CAMBRIDGE, DOWNING STREET, CAMBRIDGE CB2 3EQ, UK
[3]DEPARTMENT OF EARTH SCIENCES, UNIVERSITY OF OXFORD, SOUTH PARKS ROAD, OXFORD OX1 3AN, UK

RECEIVED SEPTEMBER 16, 2013; ACCEPTED MAY 30, 2014
ADVANCE ACCESS PUBLICATION JULY 1, 2014

The Tertiary Skaergaard intrusion, East Greenland, intruded at the shallow crustal unconformity between Precambrian amphibolite-facies gneisses and overlying Tertiary Plateau Basalts. Maximum contact metamorphic temperatures in quartzo-feldspathic gneisses were determined in two sample traverses across the aureole on the western contact of the intrusion using a combination of microstructural observations (both optical and cathodoluminescence) and the titanium-in-quartz (TitaniQ) thermometer. The onset of recrystallization of the quartz in the gneisses occurred between 390 and 340 m from the contact whereas H_2O-fluxed melting occurred in gneisses closer than 130 m from the contact (where $T > \sim 675^{\circ}C$). The maximum temperature recorded by quartz at the contact is $\sim 865 \pm 70^{\circ}C$. Melt fractions reach 50–60 vol. % in some samples although the melt is heterogeneously distributed on all scales. Minor bands of amphibolite-facies mafic gneiss are extensively reacted to an anhydrous pyroxene-bearing hornfels close to the contact, whereas those further than ~130 m are overprinted by a greenschist-facies assemblage. Discrepancies between the expected temperature for the amphibolite- to greenschist-facies reaction and temperatures obtained from adjacent quartzo-feldspathic gneisses are consistent with the formation of the anhydrous pyroxene hornfels directly from the mafic gneiss, with the lower-grade greenschist-facies assemblage forming on the retrograde path after the establishment of limited hydrothermal activity. It is unlikely that devolatilization reactions in the gneiss produced sufficient H_2O to account for the pegmatitic features formed in the Marginal Border Series in the intrusion. A simple one-dimensional thermal model, neglecting any advection of heat by hydrothermal circulation, was fitted to the profile of maximum temperature through the aureole. The generally lower temperatures seen in the gneiss compared with those previously reported for the contact metamorphosed basalts higher up the walls of the intrusion are consistent with a heterogeneous release of latent heat of crystallization.

KEY WORDS: *metamorphic aureole; Skaergaard; cathodoluminescence; titanium-in-quartz thermometry*

INTRODUCTION

Determining the thermal history of igneous intrusions is an essential step in constraining the time-scales controlling magma fractionation, eruptive behaviour, the formation of ore deposits and the thermodynamics of natural mineral assemblages. Cooling rates can be obtained from igneous rocks via the length-scales of mineral exsolution (e.g. Miyamoto & Takeda, 1994), crystal grain size (e.g. Cashman, 1993) or the geometry of three-grain junctions (Holness *et al.*, 2012). Studies of well-exposed contact aureoles can also be used to constrain thermal time-scales (e.g. Manning *et al.*, 1993; Cook & Bowman, 1994; Ferry, 1996; Müller *et al.*, 2008), determine the extent of crustal assimilation, and assess the degree to which the country rock may have supplied water to the magma, with potential effects on the liquid line of descent.

The Skaergaard intrusion of East Greenland is one of the best natural laboratories in which to study processes involved in the differentiation of mafic magma, including compaction (Tegner *et al.*, 2009; McKenzie, 2011), liquid immiscibility (Jakobsen *et al.*, 2005; Holness *et al.*, 2011) and the formation of ore deposits (Bird *et al.*, 1991).

*Corresponding author. Telephone: +1 805-280-6431. E-mail: bufe@umail.ucsb.edu
†Present address: Department of Earth Sciences, Durham University, Science Labs, Durham DH1 3LE, UK.

Despite the excellent exposure of the gneissic and basaltic country rocks, previous work on the contact metamorphism associated with the intrusion is scarce and entirely concentrated on the basalts (Manning & Bird, 1991, 1995; Manning *et al.*, 1993). In this contribution, we focus on the contact metamorphism of the Precambrian amphibolite-facies gneisses that form the lower walls and floor of the intrusion. The extent of recrystallization and melting of the quartzo-feldspathic gneisses is constrained using detailed cathodoluminescence imaging. We also describe the effects of contact metamorphism on subordinate mafic bands in the gneisses to assess the extent to which they might have supplied H_2O to flux melting in the adjacent quartzo-feldspathic material and to examine the hypothesis that the country rocks supplied significant quantities of H_2O to the marginal regions of the intrusion (Irvine *et al.*, 1998). Finally, the Ti-in-quartz geothermometer (TitaniQ) (Wark & Watson, 2006; Thomas *et al.*, 2010; Huang & Audétat, 2012) is used to constrain the profile of maximum temperatures through the aureole and compare the results with predictions based on simple numerical models for heat flow in the Skaergaard aureole.

GEOLOGICAL SETTING

The Tertiary Skaergaard intrusion is situated on the east coast of Greenland and comprises *c.* 280 km^3 of basaltic magma that intruded at a shallow crustal unconformity between Precambrian gneisses and overlying Tertiary flood basalts into a fault-bounded magma chamber (Nielsen, 2004) (Fig. 1). The magma crystallized as a closed system, forming three sequences of cumulates (Fig. 2): the volumetrically dominant Layered Series, which crystallized upwards from the floor of the intrusion; the Marginal Border Series, which accumulated from the sides of the chamber; the Upper Border Series, which crystallized downwards from the roof (Wager & Deer, 1939). The Upper Border Series and the Layered Series meet at the Sandwich Horizon (Wager & Deer, 1939). Within each series, mineral composition varies systematically from primitive to more evolved, consistent with uninterrupted fractional crystallization (Wager & Brown, 1968). Boundaries between mineral assemblages divide the Layered Series into the Hidden Zone (HZ), Lower Zone (LZ), Middle Zone (MZ) and Upper Zone (UZ) (Wager & Deer, 1939; Fig. 2), with equivalent subdivisions for the Marginal Border Series (Hoover, 1989) and Upper Border Series (Salmonsen & Tegner, 2013).

The depth of burial of the intrusion increased during its solidification history because of continued eruption of flood basalts at the surface. Larsen & Tegner (2006) estimated that the pressure at the intrusion roof increased from $0{\cdot}07 \pm 0{\cdot}05$ GPa during solidification of the lower part of LZ to $0{\cdot}33 \pm 0{\cdot}13$ GPa during solidification of the SH.

The Precambrian gneisses forming the lowermost walls and floor of the intrusion are mainly tonalitic to granitic orthogneisses, with minor mafic and ultramafic bands and rare metasediments (Kays *et al.*, 1989). Up to four pre-Tertiary regional metamorphic events are recognized, with metamorphic peaks reaching amphibolite facies and extending locally into lower granulite facies (Kays *et al.*, 1989). Large-scale pre-Tertiary anatexis was widespread and associated with strong regional deformation. In the two areas investigated for this study, mafic bands form ~5% of the predominantly quartzo-feldspathic country rock, oriented approximately east–west, parallel to the main regional fabric (shown schematically in Fig. 1). These bands are continuous over many tens of metres and are 0·5–20 m thick. The mafic bands are mainly coarse-grained hornblende–plagioclase gneisses, although some contain variable quantities of clinopyroxene. The Skaergaard intrusion caused localized remelting and mobilization of the migmatitic gneisses that is visible in outcrop within ~20 m of the contact with the intrusion.

Contact metamorphism of the basaltic rocks that form the upper walls and roof of the magma chamber resulted in the development of three zones, defined by the presence of actinolite + chlorite (>250 m from the contact), clinopyroxene + orthopyroxene (10–250 m from the contact), and olivine (<10 m from the contact) (Manning & Bird, 1991, 1995; Manning *et al.*, 1993). Rocks in the pyroxene and olivine zones have granoblastic polygonal microstructures whereas basalts from the actinolite + chlorite zone retain relict igneous microstructures (Manning & Bird, 1991). Peak contact metamorphic temperatures, determined from two-pyroxene thermometry and homogenization of fluid inclusions, range from ~900°C at the contact to 300–500°C at the edge of the aureole (Manning *et al.*, 1993). The variability of temperatures derived from two-pyroxene thermometry suggests that chemical equilibrium was attained only within 100 m of the contact during the metamorphic peak. The sharply defined transition between the pyroxene and actinolite + chlorite zones (with no intervening hornblende zone) represents a significant apparent step-wise temperature change and is consistent with non-progressive metamorphism (Manning *et al.*, 1993; Manning & Bird, 1995).

Taylor & Forester (1979) present a detailed oxygen and hydrogen isotope study of the hydrothermal system associated with the Skaergaard intrusion. The intensely jointed and fractured basalts that form the roof and upper walls display significant reductions in $\delta^{18}O$ attributable to equilibration with meteoric fluids during hydrothermal circulation. In contrast, the gneiss has unaltered oxygen isotope ratios except within a few metres of the contact and in localized regions associated with major fractures. However, the intrusion itself, the gneiss, and the plateau basalts have very low D/H values demonstrating that at

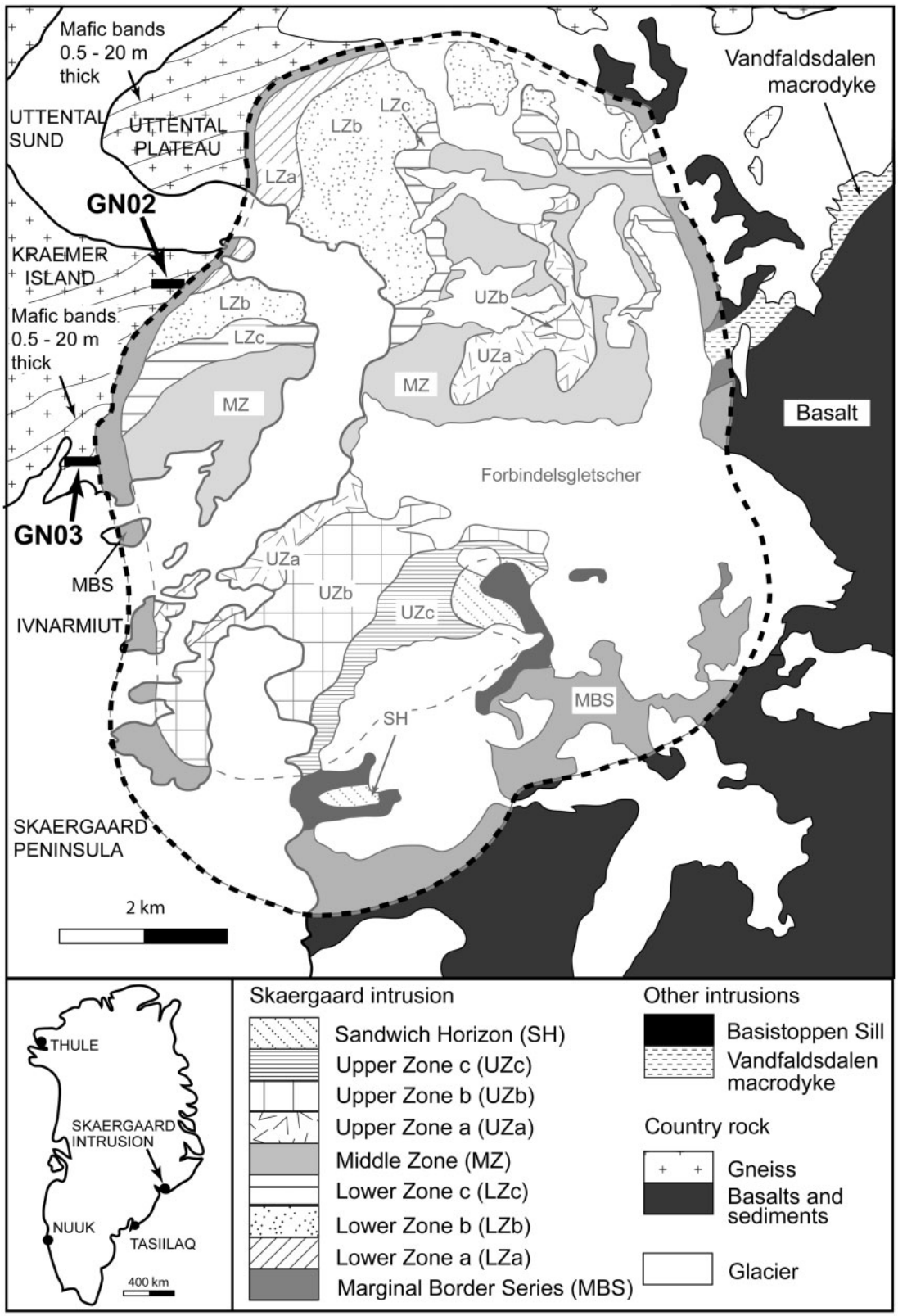

Fig. 1. Geological map of the Skaergaard intrusion and surrounding country rocks modified from McBirney (1989). Bold dotted line marks the approximate boundary of the intrusion. Thick black bars denote the location of the sample traverses.

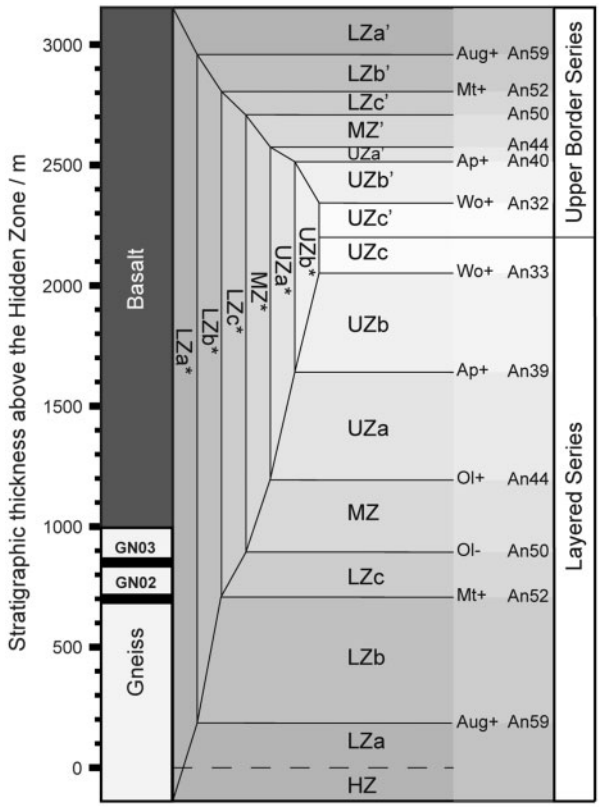

Fig. 2. Stratigraphy of the Skaergaard intrusion and the country rocks modified from Salmonsen & Tegner (2013). The subdivisions are based on the presence or absence of cumulus phases and are referred to as Hidden Zone (HZ), Lower Zone (LZ), Middle Zone (MZ) and Upper Zone (UZ). The white and dark grey zones on the left mark the approximate position of the Precambrian gneisses and overlying Tertiary basalts with respect to the layers of the intrusion. The stratigraphic heights of the sample traverses are marked by black bars. The height of the gneiss–basalt contact and the location of the traverses have an uncertainty of ±0·7 km.

least small amounts of meteoric water circulated in the Precambrian basement gneiss as well as in the overlying basalts. The overall water/rock ratios were most probably less than ~0·01 (Taylor & Forester, 1979). This implies that the general pattern of hydrothermal activity in the gneiss was one of significant meteoric water circulation confined to major fracture zones, with more pervasive hydrothermal exchange, involving very much smaller water/rock ratios, between the fractures.

SAMPLE LOCATIONS

The gneisses were sampled in two traverses approximately perpendicular to the western contact of the intrusion (Fig. 1). Samples of both the dominant quartzo-feldspathic gneiss and the amphibolite bands were collected from each locality. Sampling took place during two separate field seasons (2008, 2011), permitting the location of important microstructural developments to be pinpointed. We chose quartzo-feldspathic samples that contained as little mafic material as possible, and endeavoured to sample the freshest and least altered amphibolites. The amphibolites were predominantly sampled parallel to the approximately east–west trend of the regional fabric to minimize compositional variation along each traverse.

Perpendicular distances from the contact with the intrusion were measured in the field, or calculated from GPS coordinates (accurate to within ±2 m). The northern suite of 32 samples comprises a traverse extending 339 m from the contact. The southern traverse ends 391 m from the contact and includes 19 samples.

ANALYTICAL METHODS

Scanning electron microscopy

Cathodoluminescence (CL) of quartz is associated with lattice defects and trace element concentration (Smith & Stenstrom, 1965; Ramsayer *et al.*, 1988; Ramseyer & Mullis, 1990; Seyedolali *et al.*, 1997; Müller *et al.*, 2000, 2002, 2003*a*, 2003*b*; Götze *et al.*, 2001; Landtwing & Pettke, 2005; Rusk *et al.*, 2006), and comprises a number of peaks in the visible spectrum, mostly blue or red. A prominent peak at 415 nm is positively correlated with Ti concentration (Müller *et al.*, 2002, 2005; Rusk *et al.*, 2006, 2008; Spear & Wark, 2009), and this luminescence is expected to dominate parachromatic images at Ti contents >40–50 ppm (Müller *et al.*, 2000, 2002; Larsen *et al.*, 2009). The Ti content of quartz is proportional to the crystallization temperature (Wark & Watson, 2006; Thomas *et al.*, 2010). Therefore, the intensity of the quartz CL signal can potentially be used to infer the spatial distribution of quartz that crystallized at different temperatures.

Back-scattered electron (BSE) and CL images were collected using a Gatan MonoCL4 mounted on a JEOL JSM-820 scanning electron microscope (SEM) at the Department of Earth Sciences, University of Cambridge. We produced parachromatic CL images using an acceleration voltage of 20 kV, a beam current of 22 ± 3 nA and a working distance of 29 mm. The resultant greyscale images sum mineral luminescence over the complete visible spectrum.

Electron-probe microanalysis (EPMA)

Analysis of quartz was carried out using the Cameca SX-100 electron microprobe at the Department of Earth Sciences, University of Cambridge. A 25 kV acceleration voltage and a focused beam were used, with 10 nA beam current and 27 s peak counting time for Si, and a 300 nA beam current and 60 s peak counting time for the trace elements Fe, Ti and Al. Analytical uncertainties are given in the Supplementary Data (available for downloading at http://www.petrology.oxfordjournals.org), and were typically <25 ppm for Ti, <150 ppm for Fe and <15 ppm for Al.

Analyses with totals outside the range 98–102 wt % were discarded.

The minor element (Fe, Al, Ti) compositions of the various types of quartz were analysed using the CL images as a guide to estimate the range of crystallization temperatures (as inferred from Ti-in-quartz thermometry) for each sample. Data from the quartz types were acquired but no attempt was made to obtain statistically representative populations. In each sample, the brightest luminescent quartz was measured to record the highest titanium content.

Image preparation and analysis

CL and BSE images were stitched together in Corel Draw and Adobe Illustrator to create maps covering large areas of each thin-section. ImageJ (Schneider *et al.*, 2012) was used to quantify mineral modes on BSE images. To compare trace element concentrations with luminescence brightness, the greyscale of the CL images was calculated using ImageJ within a ~5 μm radius in the vicinity of each probe analysis point.

PETROGRAPHIC DESCRIPTIONS

Kays *et al.* (1989) have described the petrography, structure and regional metamorphism of the gneissic basement in this part of East Greenland. Here we summarize the observed microstructural and petrographic changes within the thermal aureole of the Skaergaard intrusion.

Amphibolites

The samples of amphibolite furthest from the contact are heavily hydrothermally altered, with almost complete replacement of plagioclase feldspar by turbid carbonate-rich material. Primary brown–green pleochroic hornblende and clinopyroxene (Fig. 3a) are replaced to variable extent, with the most complete replacement occurring in the vicinity of millimetre-width calcite–epidote–chlorite veins. The amphibole is replaced by a very fine-grained aggregate of sheet silicates further than 300 m from the contact but in rocks closer than 250 m, amphibole is variably replaced by actinolite + chlorite + epidote (Fig. 3b and c). Where replacement is complete, albite neoblasts are prominent. The extent to which this greenschist-facies assemblage has overprinted the amphibolite is highly variable between samples, consistent with the necessity of adding externally derived H_2O as a reactant (Elmer *et al.*, 2006). The numerous greenschist-facies veins suggest that the H_2O permeated the gneiss along fractures. This lower-grade greenschist-facies assemblage is not present in samples close to the contact.

Within ~150 m of the contact in the northern traverse, but only within ~100 m of the contact in the southern traverse, the hornblende of the amphibolite is pseudomorphed to variable extent by a fine-grained aggregate of pyroxenes, oxides ± biotite, whereas coexisting original pyroxenes are unaffected (Fig. 3d). The grain size of this replacement assemblage increases towards the contact. Plagioclase loses its turbidity about 200 m from the contact in both traverses and is generally fresh and unaltered in the pyroxene hornfelses. The presence of relict amphibole in many samples (now brown–brown pleochroic, rather than brown–green) attests to the incompleteness of this replacement. The absence of any relicts of the lower-grade greenschist-facies assemblage demonstrates that contact metamorphism of these hornfelses involved reaction of the protolith directly to the peak metamorphic assemblage. Hornblende is entirely replaced by pyroxenes and oxides within 30 m of the contact (Fig. 3e). Where quartz was present in the protolith, pockets of small euhedral plagioclase grains poikilitically enclosed by quartz are present within about 150 m of the contact on the northern traverse (Fig. 3f). We interpret this microstructure as crystallized melt. The location of the melt-in isograd along our sample traverse in the amphibolite is not well constrained by our sample set.

Quartzo-feldspathic gneisses

Far from the intrusion, the quartzo-feldspathic orthogneisses have a weak to moderate modal banding, defined by a preferred orientation of centimetre-scale lensoid aggregates of quartz and feldspar. Far-field samples contain two feldspars, oligoclase and a potassium feldspar, both of which are generally turbid, although the alkali feldspar is always more turbid than the plagioclase. Turbidity is not a general feature of the Precambrian gneisses in this region (Kays *et al.*, 1989), suggesting that our furthest sample, at 390 m, was affected by hydrothermal circulation triggered by the Skaergaard intrusion: our suite of samples therefore does not include wholly unaltered gneisses. Perthitic and anti-perthitic exsolution lamellae in the alkali feldspar are commonly <10 μm wide but can be as wide as 200 μm. Microcline is present 390 m from the intrusion. Localized bending and distortion of plagioclase twins as well as undulose extinction of quartz are evidence of deformation. The quartz grain size varies between <0·1 mm and 1 mm and is generally smaller than the size of feldspar grains. The quartz forms clusters of multiple grains and the size of the clusters is generally commensurate with the size of neighbouring feldspar grains. Minor phases include 1–10 vol. % biotite (further than about 70 m from the contact biotite is invariably completely replaced by chlorite ± titanite) and a few volume per cent Fe–Ti oxide minerals. Apatite is an accessory phase. No rutile was found. Small myrmekitic intergrowths are present in several samples.

Patches of pre-Tertiary crystallized melt are coarse-grained, with rounded quartz grains separated by thin sheets of turbid feldspar with low dihedral angles (see Holness & Sawyer, 2008). This phase of melting can be

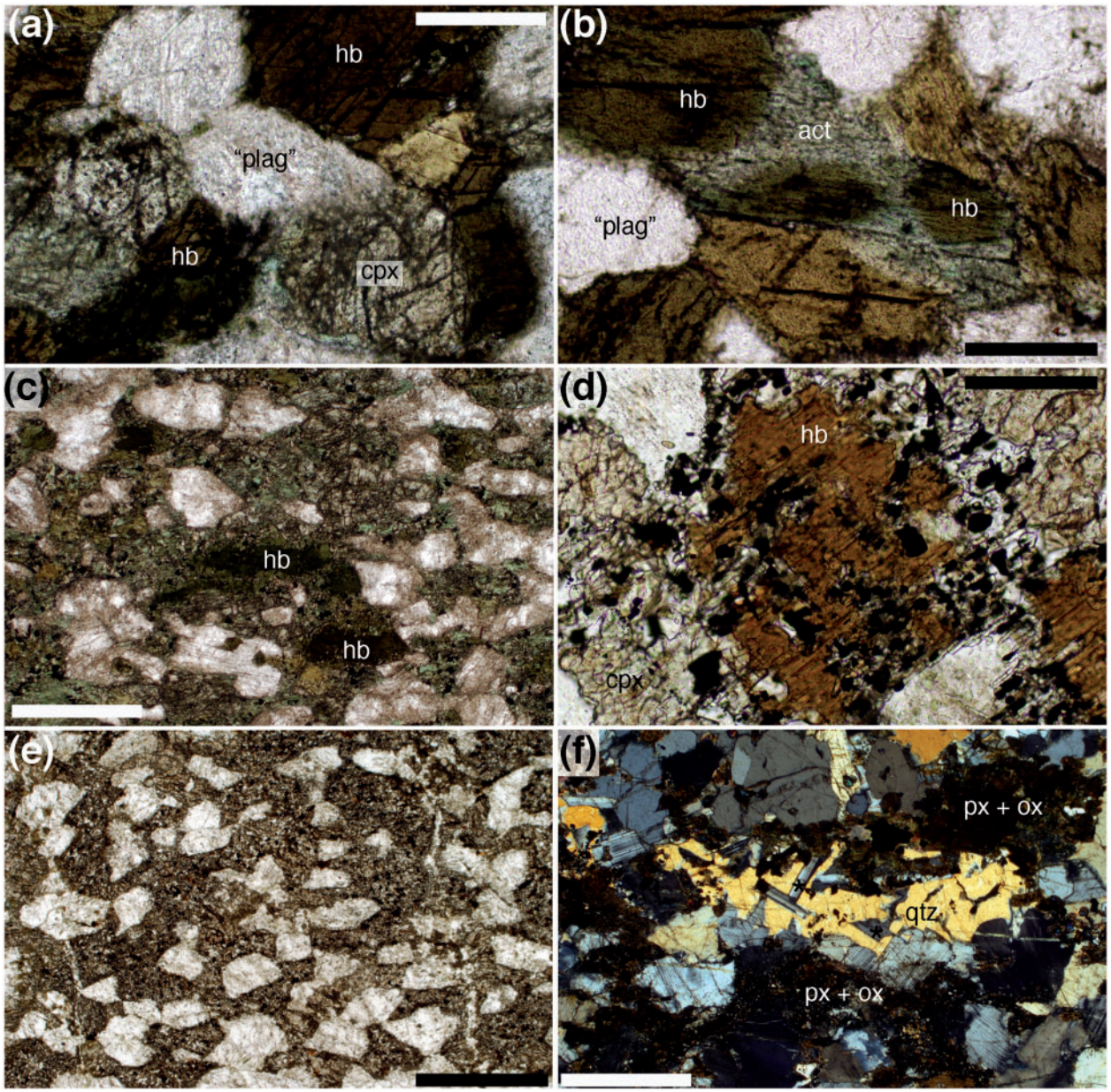

Fig. 3. Photomicrographs of contact metamorphosed amphibolites. (a) Sample GN03-17A (289 m from contact). Coarse granular brown–green pleochroic hornblende (hb) and pale green clinopyroxene (cpx) are fresh, whereas the plagioclase is replaced by a fine-grained turbid intergrowth of sheet silicates ('plag'). Plane-polarized light, scale bar represents 200 μm. (b) Sample GN03-14A (191 m from contact). The primary amphibolite-facies hornblende is locally replaced by pale green actinolite (act), in optical continuity with the hornblende. Plane-polarized light, scale bar represents 200 μm. (c) Sample GN03-11A (119 m from contact). Almost all the hornblende is pseudomorphed by a fine-grained intergrowth of actinolite and chlorite. Plane-polarized light, scale bar represents 1 mm. (d) Sample GN03-6A (57 m from contact). The hornblende is now brown–brown pleochroic and is being replaced from the edges inwards by a granular mix of oxides and pyroxene. Plane-polarized light, scale bar represents 200 μm. (e) Sample GN03-7A (70 m from contact). All hornblende grains are pseudomorphed by a granular mix of oxides and pyroxene. Crossed polars, scale bar represents 1 mm. (f) Sample GN03-4A (28 m from contact). A solidified pocket of anatectic melt marked by unstrained quartz (qtz) that encloses numerous euhedral laths of plagioclase (two of which are marked by an asterisk). The hornblende is entirely replaced by pyroxenes and oxide (px + ox). Crossed polars, scale bar represents 1 mm.

distinguished from the later contact metamorphic event by evidence of strain in both quartz and feldspar.

Under CL two types of regional metamorphic quartz (both with undulose extinction) can be distinguished (Fig. 4a and b): Qtzla is volumetrically dominant and has a chaotically mottled appearance, with micrometre-scale luminescent lines, spots and patches of varying brightness. Qtzlb is less abundant and is very weakly luminescent,

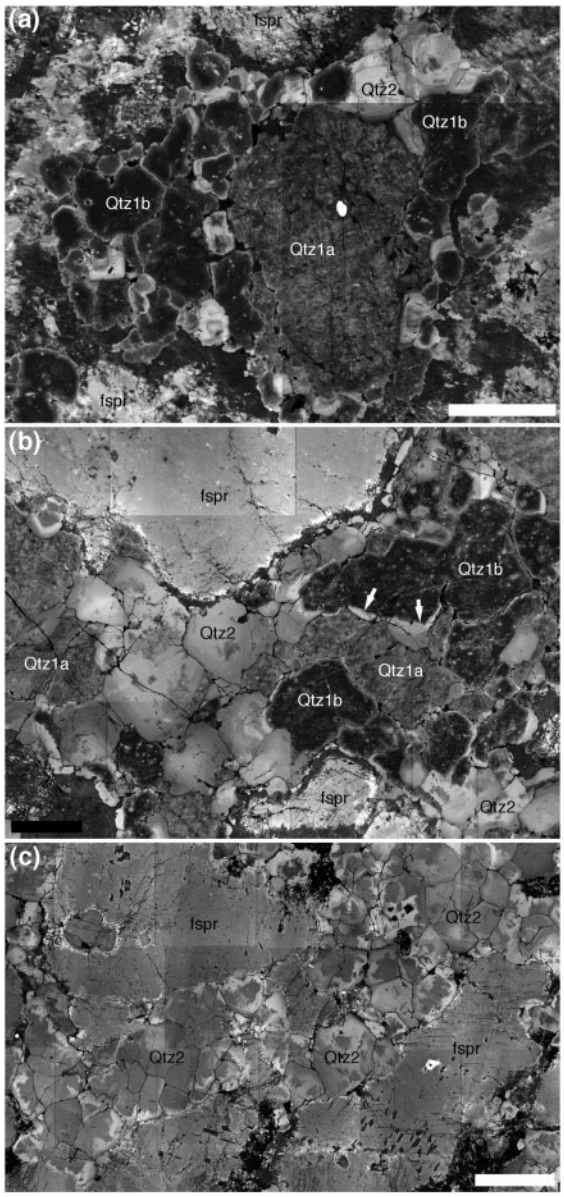

Fig. 4. Quartzo-feldspathic gneiss imaged using cathodoluminesence. (a) Sample GN02-28. The image is dominated by a large grain of Qtzla, with low luminescence and mottling. This grain is mantled by many smaller rounded grains of Qtzlb, characterized by dark luminescence with scattered bright spots. The margins of the Qtzlb grains typically are bright. A patch of several relatively bright Qtz2 grains is labelled. It should be noted the small-scale zoning visible in Qtz2 and approximately parallel to the grain boundaries. The two grains of Qtzlb immediately adjacent to the patch of Qtz2 have bright rims indistinguishable from Qtz2, indicating Tertiary regrowth of Qtzlb. Feldspar (fspr) does not strongly luminesce in this sample. Scale bar represents 500 μm. (b) Sample GN03-8. Grains of both Qtzlb and Qtz2 (labelled) replacing an older grain of Qtzla (labelled). The upper Qtzlb grain has bright margins (arrowed) formed during Tertiary contact metamorphism. Scale bar represents 500 μm. (c) Sample GN03-7. The quartz in this view is entirely of Qtz2, formed during Tertiary recrystallization. The irregular luminescence of the quartz, with relatively dark centres and banded margins, should be noted. The bands approximately parallel the present grain boundaries, suggesting they formed during grain growth. Scale bar represents 1 mm.

either entirely dark or with bright spots typically 5–30 μm in diameter and 10–100 μm apart. The grain size of Qtzlb is almost invariably smaller than that of Qtzla-type. The Qtzlb grains tend to be rounded with smooth boundaries, and the grains form aggregates within or on the margins of the Qtzla-type grains (Fig. 4a). Grains with dark Qtzlb luminescence commonly have relatively bright luminescent rims (Figs 4a and b). Both types of Qtzl have undulose extinction and are therefore interpreted to pre-date contact metamorphism.

The first indication of contact metamorphism as the intrusion is approached occurs between 390 and 330 m from the contact, where microcline becomes disordered sanidine. Subsolidus recrystallization of the original quartz also begins between 390 and 340 m from the contact and is increasingly evident closer to the intrusion. New strain-free grains (Qtz2) nucleate at quartz–feldspar grain boundaries (Fig. 5a and b) and replace the strained quartz. The shape and grain size of these strain-free grains, and their distribution on the margins of Qtzla grains, is similar to that of Qtzlb grains.

Recrystallization of Qtzla is largely complete by 290 m in the northern traverse and 180 m in the southern traverse. However, some strained quartz commonly remains, especially in the centres of large polycrystalline quartz regions even 2 m from the intrusive contact. Qtz2 has a distinctive character under CL, with a moderately luminescent core and a more luminescent rim (Fig. 4a–c). Where they coexist, the bright rims on Qtzlb are commonly widest where they are adjacent to Qtz2 grains (Fig. 4a and b). The outermost parts of Qtz2 grains generally have fine-scale oscillatory zoning, with a pattern related to present-day grain boundaries (Fig. 4c). This microstructure has previously been interpreted as a record of grain growth during contact metamorphism (Lind, 1996; Holness & Watt, 2001; Harris *et al.*, 2003; Piazolo *et al.*, 2005). The brightness of quartz with Qtz2-type luminescence is similar to that of Qtzla where it first appears but increases as the contact is approached.

About 130 m from the intrusive contact (for both the northern and the southern traverses) the feldspar grains develop a thin, highly turbid rim (Fig. 5c) although in places the newly crystallized feldspar is non-turbid (Fig. 5g). These rims are associated with the development of a highly cuspate morphology of quartz–feldspar grain boundaries (Fig. 5d–h), with an extensive network of feldspar sheets extending in optical continuity from the adjacent feldspar grain along both high- and low-angle quartz grain boundaries—these features have previously been interpreted as the result of crystallization of melt films on quartz–feldspar grain boundaries (Platten, 1982; Holness & Clemens, 1999; Holness & Watt, 2001, 2002; Holness & Isherwood, 2003; Holness & Sawyer, 2008). Under CL the quartz that crystallized from these melt films is brightly

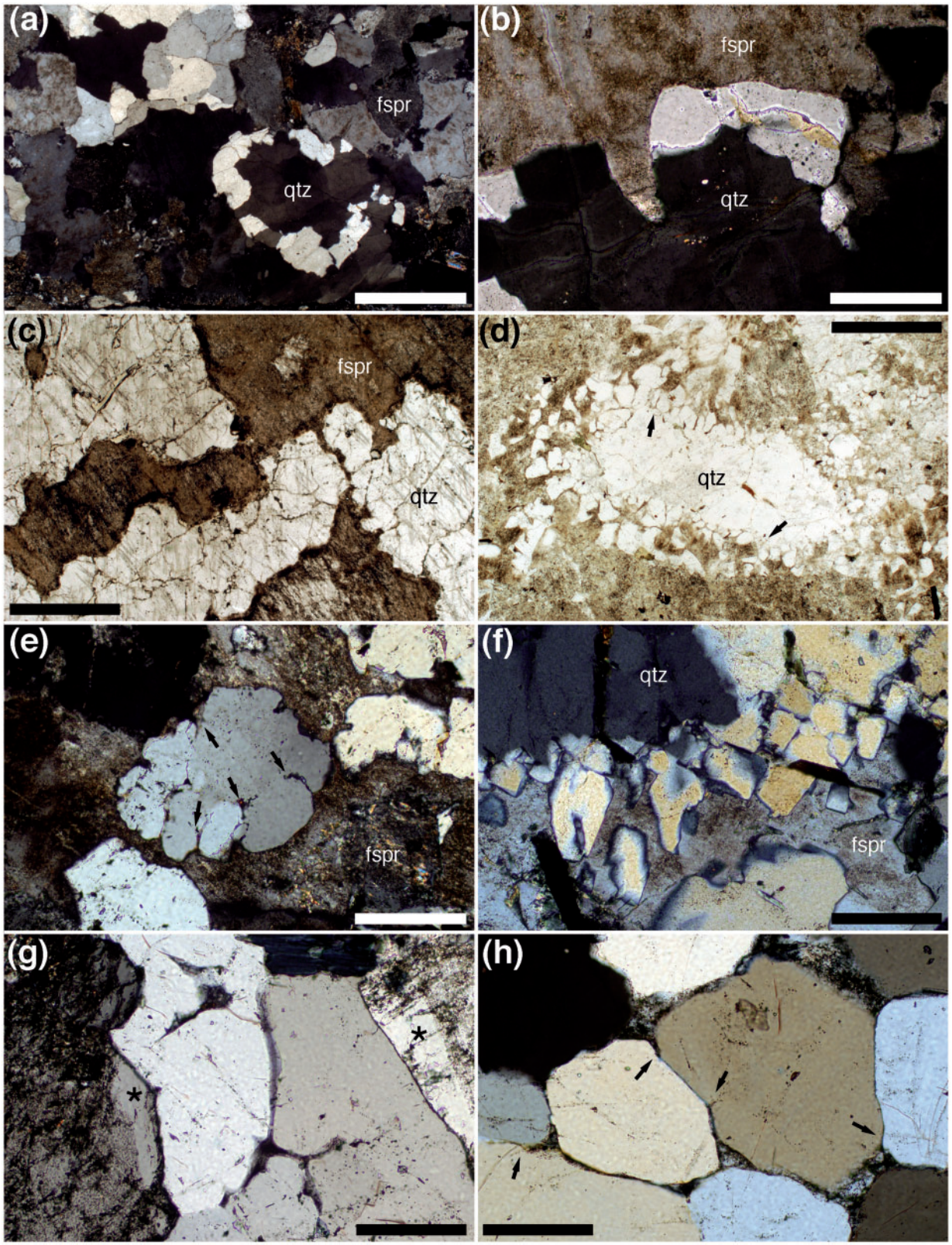

Fig. 5. Optical photomicrographs of quartzo-feldspathic gneiss. (a) Sample GN03-19. The strained amphibolite-facies Qtz1a quartz grain (labelled) is partially replaced by strain-free rounded grains of Qtz2 that nucleate on the quartz–feldspar (fspr) grain boundary and grow

(continued)

luminescent (Qtz3, Fig. 6) although luminescence may decrease towards the feldspar wall (Fig. 6a). The boundary between the Qtz3 overgrowth and the quartz grain forming the original wall of the (now crystallized) melt film is invariably smoothly rounded (Fig. 6b). With an optical microscope it is possible to identify solidified melt films with certainty only in rocks that experienced a high degree of melting, but the very distinctive CL signature of Qtz3 makes it possible to discern the former presence of a few volume per cent of melt (Fig. 6).

Close to the onset of melting, crystallized melt films are not ubiquitous, with some quartz–feldspar boundaries apparently unaffected (compare Figs 4b and 6b, which are images from different parts of the same sample, separated by a few millimetres), but within a few tens of metres of the contact crystallized melt is present on nearly all interphase grain boundaries. The modal proportion of crystallized melt (estimated visually from thin sections) generally increases towards the intrusion. The observed microstructures imply that melt was confined to films on reactant grain boundaries until the proportion of melt exceeded ~30 vol. %, at which point it occupied irregular pockets, similar in size to the restitic grains. This is consistent with observations from the Glenmore plug thermal aureole, Ardnamurchan, where significant segregation occurred at > ~42 vol. % melt (Holness *et al.*, 2005).

The pockets of crystallized melt generally contain two distinct feldspars although one is usually dominant. Both feldspars contain irregular exsolved patches on a 10–100 μm scale. There appears to be no pattern linking the dominant composition of feldspar restite and the dominant feldspar in the melt pockets. Plagioclase-dominated pockets comprise small, randomly oriented, euhedral plagioclase grains poikilitically enclosed by quartz (Figs 7a, b and 8b) and K-feldspar. Poikilitic quartz in these pockets may display fine-scale (~10–20 μm) and complexly patterned oscillatory zoning under CL (Fig. 8b). K-feldspar dominated pockets are granophyric (Figs 7e and 8a).

In samples that have extensively melted (<25 m from the contact), the extent of Tertiary quartz recrystallization

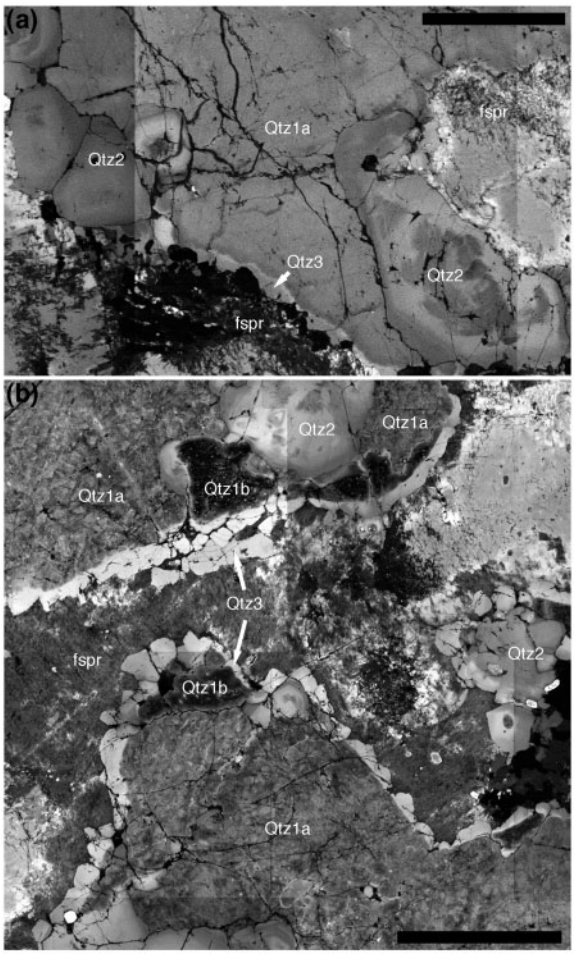

Fig. 6. Quartzo-feldspathic gneiss imaged using cathodoluminescence. (a) Sample GN03-8.5, collected 90 m from contact. Scale bar represents 500 μm. (b) Sample GN03-8, collected 82 m from contact. Scale bar represents 1 mm. The 'melt-in' isograd is close to these two samples. In (a) there is no evidence for Qtz3 on the quartz–feldspar grain boundary on the right side of the image, although there is relatively brightly luminescing quartz adjacent to the feldspar grain at the lower left (labelled Qtz3). Melting was only localized in this sample. In (b) there is a band of well-defined brightly luminescing quartz everywhere separating feldspar from quartz (labelled Qtz3), clearly indicative of ubiquitous melting on quartz–feldspar grain boundaries. The smooth boundary between the crystallized melt rim (Qtz3) and the restitic quartz should be noted.

Fig. 5. Continued
inwards from the margin of the original grain. Crossed polars. Scale bar represents 1 mm. (b) Sample GN03-19. Close-up of Qtz2 grain at the boundary between feldspar and original grain of strained quartz. Crossed polars. Scale bar represents 200 μm. (c) Sample GN02-24. The feldspar grains have turbid margins, indicative of the onset of melting during contact metamorphism. Plane-polarized light. Scale bar represents 1 mm. (d) Sample GN02-19. Solidified melt rims have formed complex intergrowths of quartz and feldspar along the boundaries of the reactant grains. The elongate extensions of feldspar into the quartz should be noted (some examples are arrowed). Plane-polarized light. Scale bar represents 1 mm. (e) Sample GN02-23. Close-up view of elongate feldspar extensions (arrowed) that grow between quartz subgrains along the margins of original quartz grains. This intergrowth of quartz and feldspar forms during solidification of melt rims. Crossed polars. Scale bar represents 200 μm. (f) Sample GN02-19. Complex, granophyric, intergrowth of quartz and feldspar that formed during solidification of a melt rim. Crossed polars. Scale bar represents 200 μm. (g) Sample GN02-22. Clear rims (marked by asterisks) on restitic feldspar grains crystallized from a melt. The cuspate and irregular (turbid) feldspar grain in the middle of the image should be noted—this grain is pseudomorphing a pore filled with crystallized melt. Crossed polars. Scale bar represents 200 μm. (h) Sample GN02-21. Cuspate grains of turbid feldspar separating rounded grains of quartz. The feldspar–quartz–quartz dihedral angle is low (examples are arrowed), indicative of crystallization in melt-filled pores. Crossed polars. Scale bar represents 200 μm.

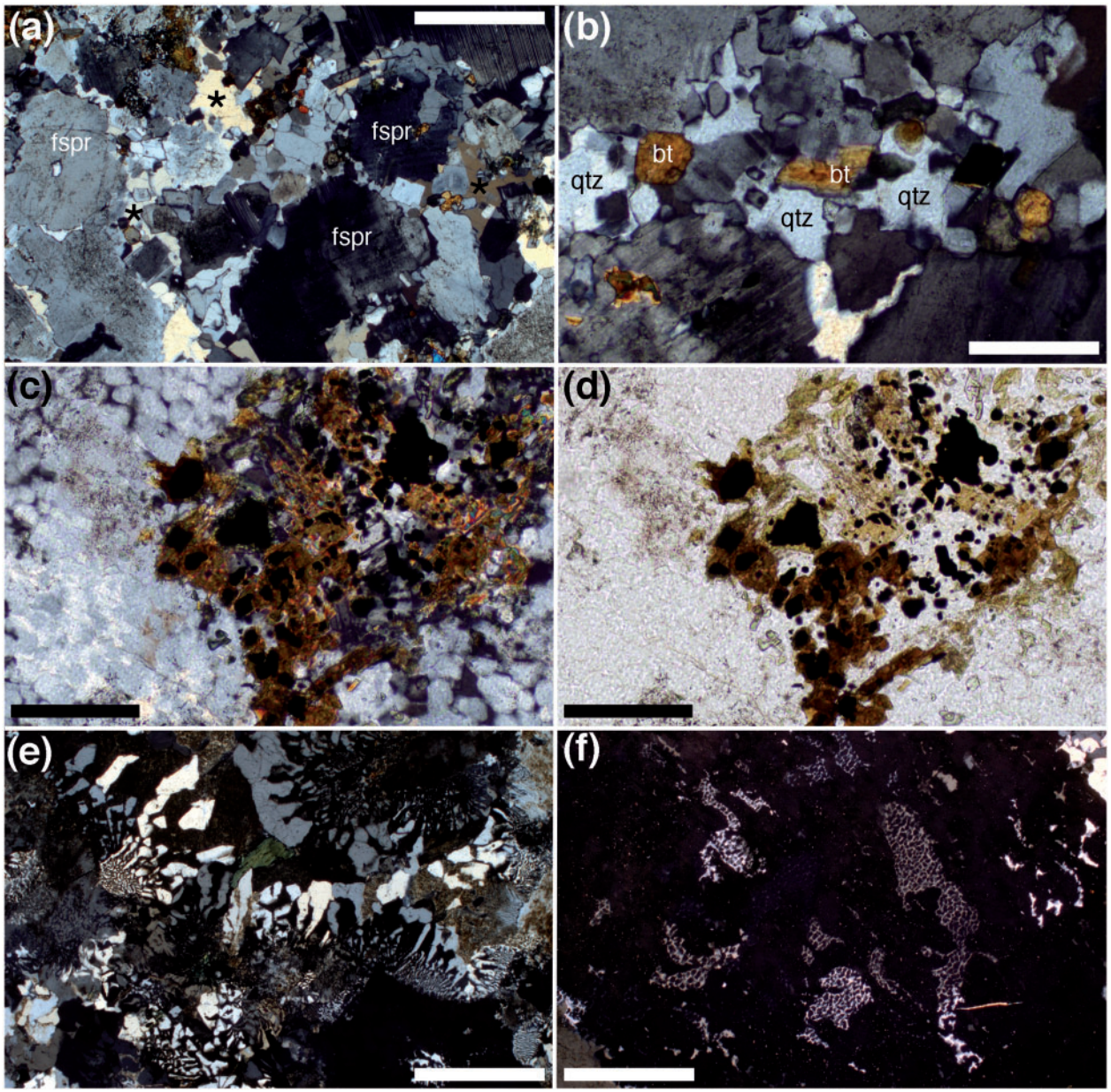

Fig. 7. Optical photomicrographs of quartzo-feldspathic gneiss. (a) Sample GN02-11. This sample contains restitic grains of feldspar (examples are labelled 'fspr'), with pools of solidified melt formed of quartz grains (marked by asterisks) enclosing small euhedral plagioclase grains. Crossed polars. Scale bar represents 1 mm. (b) Sample GN02-11. Closer view of a solidified melt pool comprising quartz (marked qtz) with included euhedral plagioclase grains. The pool also contains small brown grains of biotite (bt). Crossed polars. Scale bar represents 200 μm. (c, d) Sample GN02-14, in under crossed polars (c) and in plane polarized light (d). An original biotite grain has reacted during contact metamorphism to oxides, orthopyroxene and (inferred) melt. The partially replaced biotite grain is surrounded by sieve-textured restitic plagioclase, the holes in which are filled with quartz. Scale bar in both images represents 200 μm. (e) Sample GN03-2. Solidified melt in this sample comprises granophyric intergrowths of K-feldspar and quartz. Crossed polars. Scale bar represents 1 mm. (f) Sample GN02-13. A single grain of K-feldspar (in extinction) contains several distinct irregularly shaped pockets of sieve-texture, with isolated grains of feldspar set in quartz. The different birefringence of the quartz in each pocket shows that each comprises a single quartz grain. Crossed polars. Scale bar represents 200 μm.

(estimated by eye) is markedly less than that in non-melted samples. In these samples, the restitic quartz is therefore dominated by original regional quartz (Qtz1a and b) rather than recrystallized Qtz2 (compare Figs 4c and 8a). Extensively melted samples commonly contain both relict plagioclase and relict K-feldspar (identifiable as such from their large grain size, irregular margins and sieve texture).

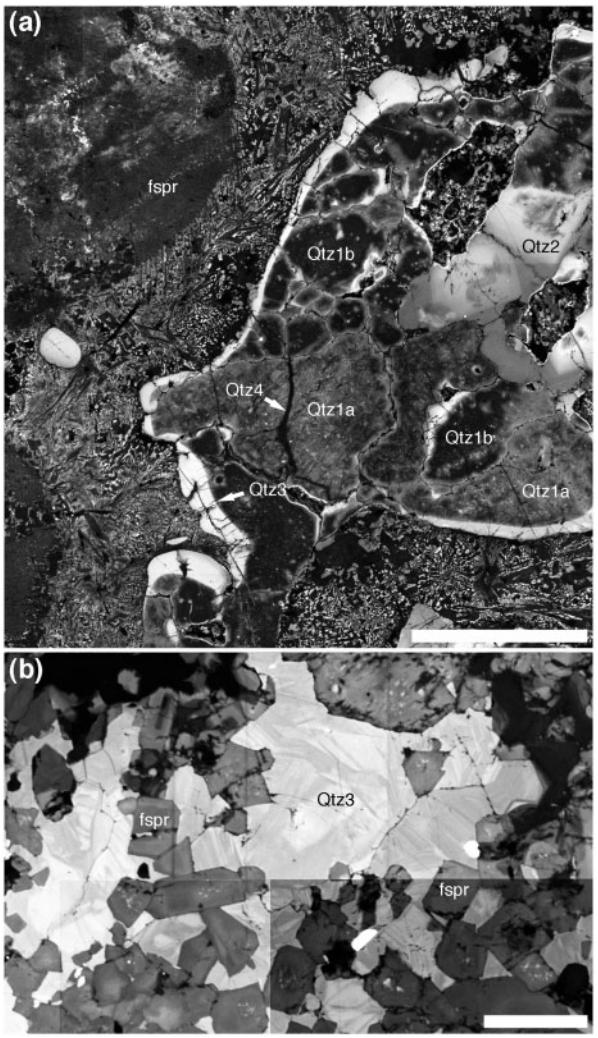

Fig. 8. Quartzo-feldspathic gneiss imaged using cathodoluminesence. (a) Sample GN03-3. A large polycrystalline aggregate of restitic quartz on the right comprises original strained and mottled quartz (Qtzla) with local pre-Tertiary replacement by Qtzlb. Tertiary contact metamorphism triggered further recrystallization with formation of grains of Qtz2. The extent of this Tertiary recrystallization was not great because the rapid heating close to the contact triggered melting at all feldspar–quartz interfaces, resulting in the formation of a thick film of melt. This crystallized to form a fine-scale granophyric intergrowth together with a brightly luminescent rim of Qtz3. The last quartz to crystallize is Qtz4—this fills non-luminescent fractures that cut all the other microstructures. Scale bar represents 1 mm. (b) Sample GN02-8. A crystallized melt pocket formed of quartz (Qtz3) enclosing euhedral grains of plagioclase feldspar. The fine-scale oscillatory zoning in the quartz should be noted. It appears to have orientations controlled by growth faces and suggests growth alternating between different faces. Scale bar represents 200 μm.

Biotite breakdown to oxides, orthopyroxene and (inferred) melt (Fig. 7c and d) occurs within 10 m of the contact. The development of the sieve texture is highly localized (Fig. 7f), suggesting that the addition of at least one reactant (H_2O?) was required for its formation. Some samples within a few metres of the contact contain almost no restitic quartz; the gneisses instead comprise rounded, partly sieve-textured restitic feldspar grains enclosed by a fine-grained mass of intergrown quartz and feldspar that we interpret as crystallized melt.

The gneiss is cut by fine veins, 1–50 μm thick, of non- or very weakly luminescent quartz (Qtz4, shown in Fig. 8a). These veins occur in all samples collected from the aureole and post-date the contact metamorphic peak (see Holness & Watt, 2002).

The main petrographic observations in the amphibolites and gneisses as a function of distance from the contact are summarized in Fig. 9.

Interpretation of microstructures

The characteristics of Qtzl, interpreted here as regional metamorphic quartz that pre-dates the contact metamorphic event, are similar to those of quartz in regional metamorphic terranes described by Lind (1996), Seyedolali *et al.* (1997), Holness & Watt (2001) and Spear & Wark (2009) (see Fig. 10 for a summary of our interpretations of the microstructures visible under cathodoluminescence). The origin of the mottled texture characteristic of Qtzla is not known, although fluid inclusions, subgrain boundaries or micro-cracks have been suggested as a cause (Lind, 1996; Watt *et al.*, 2000; Harris *et al.*, 2003). However, we found no direct correlation between intensity or distribution of mottling and the distribution of fluid inclusions, subgrain boundaries, lattice strain or microcracking.

The relative scarcity of Qtzlb grains, their spatial distribution on the margins of Qtzla grains, their rounded shape and smaller grain size suggest that they formed during post-peak partial recrystallization of an original amphibolite-facies population of large Qtzla grains. The presence of undulose extinction in both Qtzla and Qtzlb demonstrates that this recrystallization pre-dates Tertiary contact metamorphism. The preservation of low average Ti concentrations in Qtzla and Qtzlb compared with Qtz2 and Qtz3, the incompleteness of the early recrystallization event and the preservation of a later imposed undulose extinction in both Qtzla and Qtzlb suggest that temperatures generally remained low until the Tertiary contact metamorphic event.

The bright rims of the Qtzlb grains are generally widest where they are adjacent to the newly recrystallized Qtz2 grains and we suggest that these bright rims formed during a second growth phase, triggered by Tertiary contact metamorphism. The rounded shape of both Qtzlb and Qtz2 grains and the convexity of the marginal oscillatory zoning are consistent with grain growth driven by the reduction of strain energy (Vernon, 2004).

The extent of Tertiary recrystallization in the aureole is highly variable, although the most extensive recrystallization is seen in samples that lie outside the zone of partial

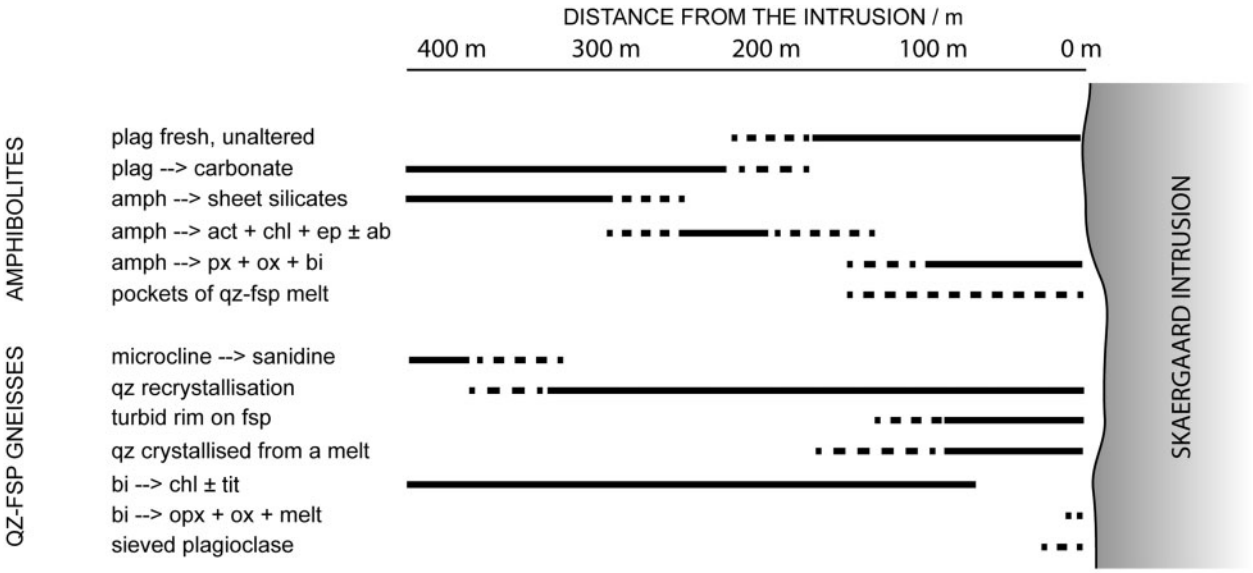

Fig. 9. A summary of the petrographic observations in amphibolite and gneisses as a function of distance from the contact. Continuous black lines mark the common presence of the observed feature. Dotted lines mark either the rare occurrence of the feature, an occurrence in only one of the traverses, or the sample gap between the last observation of the feature and the next sample. Plag, plagioclase; amph, amphibole; act, actinolite; chl, chlorite; ep, epidote; ab, albite; px, pyroxene; ox, oxide; bi, biotite; qz, quartz; fsp, feldspar; tit, titanite; opx, orthopyroxene.

Type	CL texture	Typical observations	Interpretation
Qtz1a	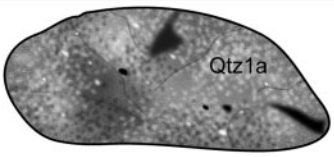	Texture: 0.2 - 3.0 mm grain size. Forms mm-cm scale polycrystalline aggregates. Undulose extinction. Luminescence: grey to dark grey. Chaotically mottled, with µm scale luminescent lines, spots and patches of varying brightness. Mottling decreases toward the intrusion, but extent of mottling is not correlated with fluid inclusion density, subgrain boundaries, lattice strain or micro-cracking.	Pre-Tertiary.
Qtz1b	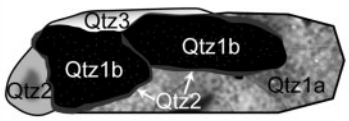	Texture: 0.1– 1.0 mm grain size. Rounded grains on margins of larger Qtz1a grains. Undulose extinction. Many grains have relatively brighter rims. Luminescence: absent or weakly mottled, with bright spots, typically 5-30 µm in diameter and 10-100 µm apart. Many grains have bright rims.	Pre-Tertiary. Strain-driven recrystallisation of Qtz1a during a pre-Tertiary event. Bright rims are likely Tertiary Qtz2.
Qtz2	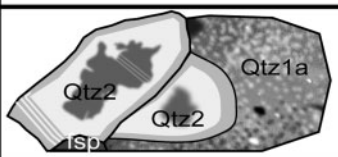	Texture: 0.1 – 1.0 mm grain size. Unstrained. Luminescence: Wide range of brightness. Cores generally dark to moderately luminescent, with a brighter rim. Cores may be patchy and/or exhibit fine zoning. Outermost rim locally darker, with fine-scale oscillatory zoning, parallel to present-day grain boundaries.	Tertiary. Recrystallisation of Qtz1a and Qtz1b during contact metamorphism.
Qtz3	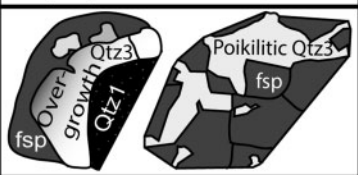	Texture: < 0.1 – 0.5 mm grain size. >25 m from contact forms overgrowths on Qtz1. < 20-25 m from contact forms oikocrysts enclosing euhedral feldspar or granophyre. Unstrained. Luminescence: Bright. Where it forms overgrowths it may have a darker rim adjacent to feldspar. Dark luminescent Qtz3 found in small pockets.	Tertiary. Crystallisation from a melt formed during contact metamorphism.
Qtz4	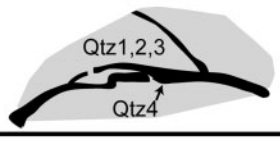	Texture: Fine µm-scale cracks within all other quartz types. Thicker and more abundant in pre-Tertiary quartz. Luminescence: Not luminescent.	Pre-Tertiary and Tertiary. Precipitated in cracks from low temperature fluids.

Fig. 10. A summary of the types of quartz distinguishable under cathodoluminescence with our interpretations.

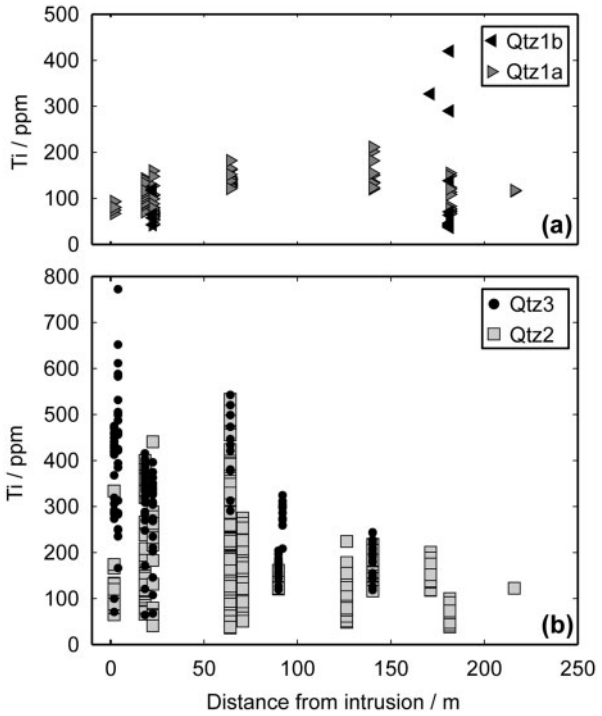

Fig. 11. Variation of Ti concentration in ppm as a function of distance from the contact and quartz type. (a) Ti concentration in Qtz1a and Qtz1b (pre-Tertiary quartz unaffected by Tertiary contact metamorphism. (b) Ti concentration in Qtz2 and Qtz3 (quartz that either recrystallized during Tertiary contact metamorphism or crystallized from melt formed during contact metamorphism). Data with titanium concentrations within three standard deviations of the detection limit were discarded and are not shown. Measurements with Al > 300 ppm and Fe > 500 ppm, as well as totals <98 wt % and >102 wt %, were also discarded.

melting. Once crystallized melt is present the restite is dominated by strained quartz. This is most probably because the temperature rose sufficiently fast that melting started before recrystallization could get properly under way. Because both processes start at quartz–feldspar grain boundaries, the melting front simply overtook the recrystallization front.

QUARTZ COMPOSITION

In each sample, the Fe and Al contents of the brightest luminescent quartz are typically in the range 0–300 ppm (with analytical 1σ variations of ±23–28 ppm (GN02-08, 18, 22; GN03-01, 03, 07, 11, 14) or ±104–108 ppm (GN02-24, 26, 28; GN03-8.5, 15) for Fe and ±4–5 ppm (GN02-08, 18, 22; GN03-01, 03, 07, 11, 14) or ±8–10 ppm (GN02-24, 26, 28; GN03-8.5, 15) for Al. (The two different sets of confidence intervals result from slightly different analytical conditions for the two sets of samples). Several analyses within 100 μm of ferromagnesian silicate grains resulted in unusually high Fe concentrations (up to 1000 ppm). We interpret this as a secondary fluorescence effect and discarded any data points with Fe > 500 ppm or Al > 300 ppm, even though we found no correlation between Fe and Al or Ti contents for these points.

Titanium concentrations range from below detection limits (~15–45 ppm) to 772 ppm, with analytical uncertainties of 7–26 ppm, and vary systematically with the petrographic type of quartz as distinguished in CL (Fig. 1l; Table 1; Supplementary Data). We exclude any points that have titanium concentrations within three standard deviations of the detection limit. The lowest Ti concentrations were found in the restitic regionally metamorphosed Qtz1, with Qtz1a containing 34–160 ppm Ti and a range in Qtz1b from below detection limits to 70 ppm. Ti concentrations in Qtz1 do not vary systematically with distance from the contact (Fig. 11a). There are three data points for Qtz1b with significantly higher Ti (Fig. 1l). No peculiarities were found either in the location of the probe points or in the concentration of other trace elements. Furthermore, the high Ti in the quartz at these points does not correlate with strong luminescence. The reason for the high Ti in the three anomalous points remains unresolved.

Ti concentrations in quartz interpreted to have grown during contact metamorphism by solid-state recrystallization of the strained quartz (Qtz2) are typically in the range 50–200 ppm (with several points reaching concentrations up to 533 ppm), and increase as the intrusive contact is approached (Fig. 11b). Quartz crystallized from the melt (Qtz3) also records a wide range of Ti concentrations, from 60 to 772 ppm. The lowest values in this range occur in all samples investigated, mostly at the outer rims of newly grown grains or in granophyre. The maximum recorded concentrations increase closer to the contact, from <330 ppm 130 m away, to >500 ppm within a few metres of the contact (Fig. 11b). For any given distance from the contact, Ti concentrations in Qtz2 and Qtz3 are generally higher in the northern traverse compared with the southern.

PRESSURE OF CONTACT METAMORPHISM

Two observations provide constraints on the pressure of metamorphism. First, the larger pools of crystallized melt contain two distinct feldspars. If equilibrium crystallization occurred from a hydrous, haplogranite melt this indicates a pressure of >0·24 GPa (Holland & Powell, 2001).

Second, mapped field relationships (McBirney *et al.*, 1989) suggest that the depth of the samples at the time of metamorphism was 2·3 ± 0·7 km below the top of the magma chamber, assuming a regional SSE tilt of 10–20° (Nielsen, 2004), with negligible stratigraphic difference between the two traverses (<200–300 m). This is equivalent to a confining pressure imposed by the overlying parts of

Table 1: Sample localities, quartz compositions and calculated temperatures of the quartzite samples

Name	Lat.	Long.	Dist. (m)	Qtz1a					Qtz1b					Qtz2					Qtz3				
				Mean Ti (ppm)*	Range Ti (ppm)	Mean *T* (°C)	Range *T* (°C)	*n*	Mean Ti (ppm)*	Range Ti (ppm)	Mean *T* (°C)	Range *T* (°C)	*n*	Mean Ti (ppm)*	Range Ti (ppm)	Mean *T* (°C)	Range *T* (°C)	*n*	Mean Ti (ppm)*	Range Ti (ppm)	Mean *T* (°C)	Range *T* (°C)	*n*
GN02-8			4·0*																442	167–772	783	666–876	24
GN02-18	68·194	31·745	18	109	70–143	619	578–648	27						173	66–400	657	572–775	49	336	64–416	748	569–781	45
GN02-22	68·194	31·747	64	139	121–182	645	631–676	22						231	36–533	686	520–817	96	427	290–543	783	732–820	11
GN02-24	68·194	31·747	92																284	209–325	729	691–747	12
GN02-26	68·194	31·749	140	157	120–211	657	630–693	9						173	116–218	668	627–696	38	191	119–244	680	629–711	24
GN02-28	68·194	31·750	171						327	327	748	748	1	142	118–201	647	628–687	62					
GN03-1	68·176	31·768	2	81	67–93	591	573–605	6						124	65–334	626	570–751	17	367	71–475	756	579–800	23
GN03-3	68·176	31·769	23	80	42–160	585	533–661	24	78	43–120	582	534–630	6	177	41–441	652	530–789	17	281	67–397	722	573–774	22
GN03-7	68·176	31·770	71											160	51–275	655	548–725	68					
GN03-8·5	68·176	31·770	90											133	121–161	641	631–662	20	164	120–204	663	630–689	16
GN03-11	68·176	31·771	126											96	49–224	603	545–700	75					
GN03-14	68·176	31·773	182	98	66–155	606	572–657	15	90	37–420	572	522–782	16	65	38–100	568	525–612	19					
GN03-15	68·176	31·774	216	116	116–117	627	626–628	2						122	122	632	632	1					

Name, name of sample; Lat., latitude of sample locality; Long., longitude of sample locality; Dist., perpendicular distance from the contact calculated from GPS points of the sample localities and GPS points of the contact. Qtz1a, Qtz1b, Qtz2 and Qtz3 are averages and range of Ti compositions (in parts per million) and calculated temperatures (in degrees Celsius) for each of the quartz types in each sample. *n*, number of measurements for that quartz type and sample. Cells are left empty when no analysis was made. *Distances measured in the field where no GPS data were taken.

the Layered Series and the UBS of $\sim 0{\cdot}07 \pm 0{\cdot}02$ GPa, assuming an average density of the overburden of $3{\cdot}2$ g cm^{-3}. Larsen & Tegner (2006) estimated that the initial pressure at the top of the intrusion was $0{\cdot}07 \pm 0{\cdot}05$ GPa, which increased to $0{\cdot}33 \pm 0{\cdot}13$ GPa over the ~300 kyr taken to solidify the intrusion as a consequence of continuous eruption of flood basalts. Combining the pressure estimate for the top of the Skaergaard magma chamber (Larsen & Tegner, 2006) with the differential overburden between the top of the intrusion and the level of our sample traverse, the pressure of contact metamorphism in our samples is likely to have increased from $0{\cdot}14 \pm 0{\cdot}05$ to $0{\cdot}40 \pm 0{\cdot}13$ GPa over the time of cooling of the intrusion. However, because the timescale of prograde contact metamorphism is short we assume that the pressure at peak metamorphism was approximately constant throughout the aureole and close to the confining pressure at the time of intrusion (i.e. $0{\cdot}14 \pm 0{\cdot}05$ GPa). This is lower than the independent pressure estimate from the presence of two feldspars in the crystallized melt pools, suggesting that the confining pressure may actually have been very close to the two-feldspar solvus. Thus, although neither of our two pressure estimates is well constrained we suggest that the pressure of metamorphism was of the order of $0{\cdot}25 \pm 0{\cdot}05$ GPa.

THERMOMETRY

Ti-in-quartz thermometer

The titanium-in-quartz (TitaniQ) thermometer exploits the temperature-dependent solubility of titanium in quartz. The original TitaniQ thermometer of Wark & Watson (2006) has subsequently been refined by Thomas *et al.* (2010) to include the effects of pressure on Ti solubility. The experimental calibration of the thermometer was made at rutile saturation with a titanium activity ($a\mathrm{TiO_2}$) of 1·0, and extrapolation to lower $a\mathrm{TiO_2}$ is achieved by a linear scaling between melt and quartz $\mathrm{TiO_2}$ content (Thomas *et al.*, 2010) or by consideration of Fe–Ti oxide compositions (Ghiorso & Gualda, 2013). Extrapolation to lower pressures than those of the experiments (<0·5 GPa) is expected to be unproblematic, as shown by close agreement with the lower pressure experiments of Ostapenko *et al.* (1987). Similarly, varying water contents are not expected to significantly influence Ti solubility in quartz (Hayden & Watson, 2007) and thus have little effect on calculated temperatures. Recently, Huang & Audétat (2012) showed that the titanium concentration in quartz increases significantly with increasing growth rate. They suggested that growth rates in the experiments of Thomas *et al.* (2010) were too fast to capture equilibrium conditions, leading to an underestimation of temperature. They recalibrated the thermometer based on the slowest grown quartz that was assumed to be closest to equilibrium. The two different calibrations by Thomas *et al.* (2010) and Huang & Audétat (2012) yield temperatures that can differ by more than 200°C at pressures of 0·2 GPa. Studies supporting both calibrations exist (Leeman *et al.*, 2012; Wilson *et al.*, 2012; Ashley *et al.*, 2013; Audétat, 2013; Morgan *et al.*, 2013; Kularatne & Audétat, 2014), suggesting that the two calibrations might be appropriate in different geological settings or that their success might be dependent on $a\mathrm{TiO_2}$ (Leeman *et al.*, 2012; Thomas & Watson, 2012; Wilson *et al.*, 2012; Morgan *et al.*, 2013; Kularatne & Audétat, 2014). It should be noted that an alternative TitaniQ calibration by Kawasaki & Osanai (2008), as well as the calibration by Wark & Watson (2006), does not include a pressure dependence and will not be included in the following discussion.

Sources of error in our temperature determinations are the uncertainty in the pressure of metamorphism and in the $\mathrm{TiO_2}$ activity, and the uncertainties pertaining to the calibration of the thermometer. The errors introduced by the uncertainty in pressure are negligible relative to the uncertainties relating to crystal growth rates (which are essentially unknown during contact metamorphism) and $a\mathrm{TiO_2}$. Our samples do not contain rutile, so we can be sure that $a\mathrm{TiO_2} < 1$, but they do contain Fe–Ti oxides, which should fix $a\mathrm{TiO_2}$ at some intermediate value during subsolidus quartz crystallization (Qtz2) (e.g. Ghiorso & Gualda, 2013), assuming that equilibrium can be achieved (see Huang & Audetat, 2012; Morgan *et al.*, 2013). For melt-present crystallization, several studies demonstrate that in silicic volcanic systems, $a\mathrm{TiO_2}$ typically varies by <0·5 between compositionally similar samples from the same location (Leeman *et al.*, 2012; Audétat, 2013; Ghiorso & Gualda, 2013; Kularatne & Audétat, 2014). These studies are not directly applicable to a contact metamorphic setting where melt fractions are significantly smaller. However, following a similar argument as above for Qtz2, $a\mathrm{TiO_2}$ of quartz crystallized from a melt (Qtz3) in the Skaergaard aureole should also vary little if the melt were in equilibrium with the Fe–Ti oxides and if melting did not involve the oxides. We note a lack of petrographic evidence for melting of the oxides. Thus the titanium activity may have varied between crystallization of Qtz2 (subsolidus) and Qtz3 (super-solidus) but we interpret the relative differences within each textural type to be primarily a function of variations in temperature. As we show below, this interpretation is supported by the results of other independent temperature estimates. We therefore assume that $a\mathrm{TiO_2}$ varied by <0·5 in both quartz types and across samples in the aureole. This allows us to infer relative temperature gradients throughout the aureole, with uncertainties that are largely due to unknown $a\mathrm{TiO_2}$ and growth rates. These relative temperatures can be calibrated against independent temperature estimates for the onset of melting in the aureole.

Determination of peak metamorphic temperature

Previous work has shown that determining peak metamorphic temperatures can be challenging, particularly for rocks in which grains record a wide range of temperatures. For example, use of the calcite–dolomite thermometer commonly involves choosing only those grains with the highest magnesium content to obtain the best estimate for peak temperatures, discarding those with lower magnesium contents that are assumed to have been significantly affected by retrograde re-equilibration (e.g. Holness *et al.*, 1991; Cook & Bowman, 1994; Ferry, 1996; Ferry, 2001). However, given the likelihood of at least some re-equilibration, peak temperatures determined in this way are still assumed to be minimum estimates (Holness *et al.*, 1991; Ferry, 1996, 2001; Müller *et al.*, 2008). A different treatment of a scatter of temperature values is to take the averages of the population (e.g. Manning *et al.*, 1993). This is appropriate if the compositional scatter is caused by analytical imprecision, varying degree of disequilibrium or spatially varying activities of the components.

In our samples, we observe a large range of analysed Ti contents (Fig. 11), much greater than that of the analytical uncertainty in the EPMA. This range could be caused by quartz crystallizing over a wide temperature interval during the evolution of the aureole owing to kinetic factors, such as nucleation inhibition in small melt-filled pores (e.g. Holness & Sawyer, 2008). The range might also be due to varying degrees of post-peak diffusion and re-equilibration. In both cases the highest recorded temperature in the sample would yield a minimum estimate of the peak metamorphic temperature. Finally, the range of apparent recorded temperatures could be caused by spatial and temporal variations of $a\mathrm{TiO_2}$ or growth rates, as discussed above (Huang & Audétat, 2012). If so, $\mathrm{TiO_2}$ concentrations could potentially be higher than those expected for equilibrium and be randomly distributed among quartz grains crystallized at the same temperature. In such a case it would be most appropriate to determine temperature by taking averages from a number of grains.

The clearest evidence against a random distribution of $\mathrm{TiO_2}$ concentrations in quartz is provided by the centimetre-scale CL maps (Figs 4, 6 and 8), which are composed of a number of $\sim 2\,\mathrm{mm}^2$ images that are stitched together. The luminescence varies across different images within each map owing to changes in brightness when the sample is moved in the SEM or when the contrast and brightness of the CL detector are adjusted. However, it is easy to qualitatively assess the brightness of the quartz across images by comparing it with different minerals with a more uniform luminescence in the same image. To test the relationship between quartz luminescence and Ti content (see Müller *et al.*, 2000, 2002; Larsen *et al.*, 2009), we compared trace element concentrations in quartz with the greyscale in the CL images within $\sim 5\,\mu\mathrm{m}$ of the sampled point. The results of this comparison in nine SEM-CL images from four samples are shown in Fig. 12. Owing to variations in brightness across different images in the same map, points from each image define a separate trend. However, for any single image (one set of symbols in Fig. 12), there is typically a good correlation of Ti content with brightness, particularly for images with a wide range of Ti concentrations. We are therefore confident that the brightness of the luminescence is a good overall proxy for the $\mathrm{TiO_2}$ content in the quartz of this study. The CL maps clearly show that differently luminescing quartz grains are systematically arranged through the sample, correlating with observations made using optical microscopy, and therefore argue against a random scatter of $\mathrm{TiO_2}$ concentrations (Figs 4, 6 and 8).

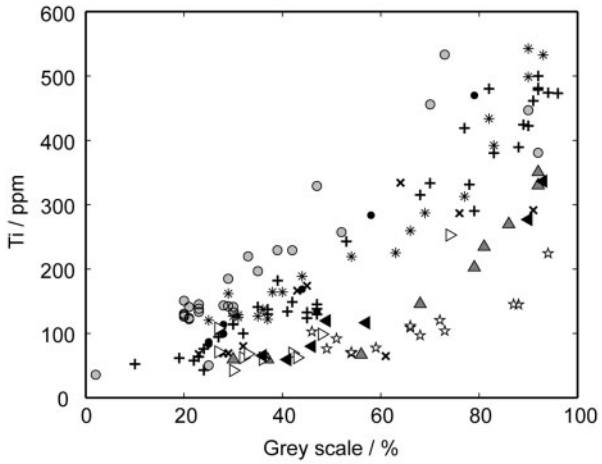

Fig. 12. Relationship between brightness of the cathodoluminescence (measured in percent greyscale from black (0%) to white (100%)) and titanium concentration in quartz for nine images in four samples. Each symbol represents a suite of greyscale–Ti-concentration pairs measured in quartz within a single cathodoluminescence image. The brightness of the cathodoluminescence varies when the sample is moved or exchanged, making comparisons between images not straightforward.

In conclusion, quartz with the highest $\mathrm{TiO_2}$ concentration in each sample can be targeted by analysing the brightest luminescent quartz. Moreover, the highest recorded Ti concentrations most probably provide the best estimate for peak temperatures. For the extraction of peak temperatures through the aureole, we therefore choose to average the highest three titanium concentrations for each quartz type with the exception of sample GNO3-15, for which only one data point was above the detection limit. We note in passing that using only the single highest temperature datum does not yield significantly different results.

Choice of thermometer and constraints on Ti activity

In addition to the TitaniQ thermometer, there are a number of equilibria that can be used to evaluate

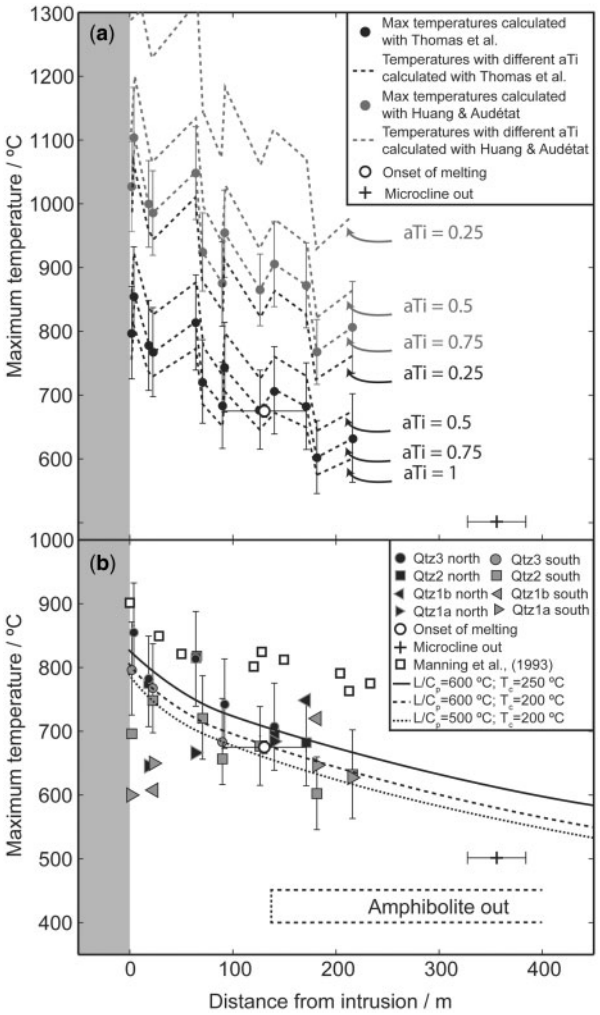

Fig. 13. Profiles of maximum temperature through the aureole calculated using the TitaniQ thermometer and temperature estimates from metamorphic reactions. (a) Plot contrasting temperatures from the TitaniQ thermometer using calibrations by Thomas *et al.* (2010) (black data points) and Huang & Audétat (2012) (grey data points) at $a\mathrm{TiO_2} = 0{\cdot}75 \pm 0{\cdot}25$ and averaging the highest three temperatures for each quartz type (see text for details). Only the highest temperatures are reported, regardless of whether both Qtz3 and Qtz2 are present. Dashed lines mark the change in calculated temperatures as the titanium activity is varied. Error bars on maximum temperature estimates denote propagated 2σ uncertainties (see text for more details). The white circle shows the likely temperature for the onset of melting in the Ab–Or–Qtz–H_2O system (Tuttle & Bowen, 1958; Holtz *et al.*, 1992; Holland & Powell, 2001) with horizontal error bars marking the distance between the first observation of melt in the southern and northern traverses. The black cross represents the conversion of microcline to sanidine, with horizontal error bars marking the distance between the two samples that bracket the transition. (b) Temperatures calculated from maximum Ti concentrations for every quartz type in each sample using the thermometer of Thomas *et al.* (2010) at $a\mathrm{TiO_2} = 0{\cdot}75 \pm 0{\cdot}25$ and averaging the highest three temperatures for each quartz type (see text for details). The error bars, the temperature from the onset of melting and the temperature from the microcline–sanidine conversion are the same as above. For clarity, uncertainties are shown for only the maximum temperature of Tertiary quartz (Qtz2 or Qtz3) in each sample. The uncertainties for the other data points are of similar magnitude.

metamorphic temperatures (Figs 9 and 13). Microcline is present in the samples furthest from the contact (390–400 m) and inverts to sanidine or orthoclase above 500°C (Smith & Brown, 1988). This transition occurs between 390 and 330 m from the contact. The onset of melting and the appearance of Qtz3 are found between 90 and 96 m in the southern traverse, and between 150 and 170 m in the northern traverse. As crystallized melt rims on quartz–feldspar grain boundaries are not pervasive, at least near the onset of melting, the melting must have been fluxed by the addition of H_2O. At $0{\cdot}25 \pm 0{\cdot}05$ GPa melting begins in the system Ab + Or + Qtz + H_2O at ~670°C, in Ab + Qtz + H_2O at ~735°C, and in Or + Qtz + H_2O at ~750°C (Tuttle & Bowen, 1958; Holtz *et al.*, 1992; Holland & Powell, 2001). The addition of anorthite (up to An_{40}) is expected to shift the melting temperatures upwards by <7°C (Johannes, 1984). Although we cannot be certain that melting was H_2O-saturated the temperature at the onset of melting is not dependent on absolute water concentration. Therefore, the temperatures of wet melting of quartzo-feldspathic rocks are applicable to the onset of melting in H_2O-undersaturated but not entirely dry rocks.

Figure 13a shows the temperature constraints from the onset of melting and the microcline–sanidine conversion together with the TitaniQ temperatures for the highest TiO_2 quartz (including only contact metamorphic Qtz2 and Qtz3) in the samples. TitaniQ temperatures are calculated with both the Thomas *et al.* (2010) and the Huang & Audétat (2012) calibration at $P = 0{\cdot}25 \pm 0{\cdot}05$ GPa and $a\mathrm{TiO_2} = 0{\cdot}75 \pm 0{\cdot}25$. As discussed above, the choice of activities is arbitrary but the variations between samples are expected to be less than 0·5.

The error bars mark propagated 2σ uncertainties incorporating the uncertainties in the experimental calibration of the thermometer [only for the Thomas *et al.* (2010) calibration, where these uncertainties are reported], in the titanium activity, in the pressure and in the electron probe measurements. The dashed lines in Fig. 13a show the variation of the temperature estimate as $a\mathrm{TiO_2}$ is varied.

Using the Thomas *et al.* (2010) calibration with $0{\cdot}5 < a\mathrm{TiO_2} < 1$ results in calculated temperatures consistent with the observed onset of melting, with the position of the disordering of microcline, and with a realistic

Fig. 13. Continued
The Manning *et al.* (1993) estimates were obtained from two-pyroxene thermometry in the basalts forming the aureole on the eastern contact. The box marked 'amphibolite out' marks the temperature and distance over which we see greenschist-facies assemblages replacing hornblende of the original amphibolite-facies mafic gneiss in both the north and south traverses. The three curves show profiles of maximum temperature calculated from the thermal model. The lowest corresponds to $L/C_p = 500$°C and an initial country rock temperature of 200°C, the middle curve corresponds to $L/C_p = 600$°C and a country rock temperature of 200°C, and the top curve corresponds to $L/C_p = 600$°C and a country rock temperature of 250°C.

temperature at the intrusion contact (Fig. 13a). In contrast, the temperatures calculated using the calibrations from either Wark & Watson (2006) or Huang & Audétat (2012) are ~150–200°C higher (Fig. 13a), and inconsistent with our independent temperature estimates. This difference cannot be accounted for by an inaccurate pressure estimate, as reducing pressure to the clearly unrealistic value of 0·01 GPa reduces calculated temperatures only by less than 100°C. Similarly, the difference cannot be accounted for by an inaccurate estimate of titanium activity. Even if we assume $a\mathrm{TiO_2}=1$, to obtain the lowest possible temperature estimate, only the Thomas *et al.* (2010) calibration is consistent with our petrographic observations (Fig. 13a). However, lowering the activity to below 0·5 makes even the Thomas *et al.* (2010) calibration inconsistent with the petrography.

Further support for temperatures calculated with the Thomas *et al.* (2010) calibration with $a\mathrm{TiO_2}=0{\cdot}75\pm0{\cdot}25$ is provided by sample GN03-7. Whereas most of our samples contain both plagioclase and K-feldspar, GN03-7 is tonalitic, with <2 vol. % K-feldspar. This sample contains no detectable crystallized melt despite being only 71 m from the contact with the intrusion. Ti-in-quartz thermometry provides a maximum temperature of 721 ±65°C for this sample, just below the $\mathrm{Ab+Qtz+H_2O}$ solidus at ~735°C (Tuttle & Bowen, 1958; Holtz *et al.*, 1992; Holland & Powell, 2001). Thus, the temperatures for the onset of melting are consistent not only with our calculated temperatures for quartz interpreted to have crystallized from a melt (Qtz3), but also with the presence of microstructures commonly associated with water-fluxed melting and with the apparent absence of crystallized melt in some samples close to the contact. A summary of the data is presented in Table 1, with the complete dataset in the Supplementary Data.

Ti-in-quartz thermometer results

Figure 13b shows maximum temperatures measured in all quartz types using the Thomas *et al.* (2010) calibration with $a\mathrm{TiO_2}=0{\cdot}75\pm0{\cdot}25$. Whereas there is no consistent variation of maximum calculated temperatures with distance from the contact in Qtz1 (see Fig. 13b), the maximum calculated temperature in both Qtz2 and Qtz3 increases as the contact is approached, from 611 ±57°C to 876 ± 80°C (Fig. 13b). This observation is consistent with the interpretation that Qtz1 represents the earlier regional metamorphism and has mostly been unaffected by the contact metamorphism, whereas Qtz2 and Qtz3 are products of recrystallization and crystallization from a melt during the contact metamorphic event. As discussed above, a direct comparison between Qtz2 and Qtz3 might be difficult owing to different $a\mathrm{TiO_2}$ during these two processes, but the increase of temperature towards the aureole is still apparent even if the quartz types are considered in isolation.

Temperatures calculated for the complete range of measured titanium concentrations (Fig. 11) are <533 to 693 ± 68°C for Qtz1a, <522°C to 782 ± 71°C for Qtz1b, <520°C to 817 ± 74°C for Qtz2, and 569 ± 55°C to 876 ± 80°C for Qtz3 (Table 1). The ranges of calculated temperatures in Qtz2 and Qtz3 are similar, but the generally brighter luminescence of Qtz3 suggests that the average temperature at which Qtz3 crystallized was higher than that for Qtz2.

Temperature constraints placed by metamorphic reactions

In the presence of $\mathrm{H_2O}$, the hornblende–plagioclase assemblage reacts to form the lower-temperature actinolite + chlorite + epidote + albite assemblage at temperatures below 400–450°C (e.g. Liou *et al.*, 1974; Elmer *et al.*, 2006). The amphibolite to greenschist transition therefore provides a constraint on minimum temperature in the aureole. The transition occurred in the amphibolites further than about 130 m from the contact in the southern traverse and further than 200 m in the northern traverse. The most proximal mafic samples containing the greenschist-facies assemblage are associated with quartzofeldspathic gneisses in which recrystallized quartz provides temperatures some 200°C higher than the amphibolite–greenschist transition (Fig. 13). The significance of this observation will be discussed below.

THERMAL MODELLING

Numerical modelling

We calculated the maximum temperatures reached in the aureole using a simple, single-step numerical model based on the instantaneous emplacement of a spherical intrusion. We ignored the effect of hydrothermal circulation on heat transport in the aureole, because the water/rock ratio in the gneisses was most likely to have been very low (Norton & Taylor, 1979). The heat conduction equation was solved in one dimension in spherical polar coordinates. We allowed for latent heat of crystallization by imposing an extra enthalpy that needs to be dissipated before cooling in the intrusion starts (this assumes that crystallization of the magma begins immediately after emplacement).

The thermal diffusivity, κ, of both gneisses and basalts is assumed to be 10^{-6} $\mathrm{m^2\ s^{-1}}$. We assumed a heat capacity value, C_p, of 0·7 $\mathrm{J\ g^{-1}K^{-1}}$ for both rock types. The intrusion radius was set at 4000 m (Nielsen, 2004): the corresponding volume of 270 $\mathrm{km^3}$ is close to published volume estimates of 280 $\mathrm{km^3}$. The temperature of the country rock prior to intrusion was likely to have been 200–250°C (Manning *et al.*, 1993), corresponding to a geothermal gradient of ~35°C. We assumed an initial magma temperature of 1160°C (Thy *et al.*, 2006) and an average value of the latent heat of crystallization, L, of 420 $\mathrm{J\ g^{-1}}$ (Norton &

Taylor, 1979), released homogeneously from the initial temperature to the solidus at 1000°C. Even if the distribution of latent heat was inhomogeneous, the value of 420 J g^{-1} would still be appropriate for the lower parts of the intrusion [see fig. 7 of Norton & Taylor (1979)].

The profiles of maximum temperature are shown in Fig. 13. Variations of the input values for initial country rock temperature and the effect of latent heat (with L/C_p varying between 500 and 600 K) result in variations in the profile of maximum temperature that fall within the uncertainties of the temperatures calculated using the TitaniQ thermometer. Our profiles are similar to that calculated by Manning *et al.* (1993) for a homogeneously distributed latent heat contribution of 418 J g^{-1}.

DISCUSSION

Comparison with the aureole developed in the basalts

Maximum temperatures

Two-pyroxene thermometry in the pyroxene zone of the aureole formed in the basaltic country rocks on the eastern margin of the intrusion (Manning *et al.*, 1993) yields maximum temperatures of ~900°C (Fig. 13) at the contact, decreasing to ~800°C 250 m away. These temperatures are considerably higher than those we obtained using the TitaniQ thermometer on the quartzo-feldspathic gneisses. Manning *et al.* (1993) reproduced their metamorphic temperatures within 100 m of the contact (where the pyroxenes are most likely to be in chemical equilibrium during the metamorphic peak) with a two-dimensional conduction model assuming a heterogeneous distribution of latent heat release [following Norton & Taylor (1979), who argued that the distribution of layering in the intrusion suggests that most of the heat of crystallization was released at the general level of the Sandwich Horizon]. Norton & Taylor (1979) suggested that latent heat of crystallization at the stratigraphic level corresponding to the traverse examined by Manning *et al.* (1993) was of the order of 837 J g^{-1}, thus leading to higher temperatures in the aureole at this level compared with those reached at deeper levels. The more complex model of Norton & Taylor (1979), involving heterogeneous release of latent heat together with the effects of hydrothermal circulation with strongly contrasting permeabilities of the basalts and the gneisses, results in higher temperatures being attained in the region of the Manning *et al.* (1993) profile compared with the gneisses of Kramer Island.

Non-progressive metamorphism

In the outer parts of the aureole, where the mafic bands have reacted to a greenschist assemblage, temperatures obtained using quartz thermometry in the surrounding quartzo-feldspathic gneisses are significantly higher than the temperature of the amphibolite to greenschist transition (Fig. 13). If reaction to the greenschist assemblage occurred on the prograde path, it must have happened significantly before the attainment of peak metamorphic temperatures, thus necessitating the presence of significant quantities of H_2O in the amphibolite in the early stages of metamorphism. Furthermore, the quartz thermometry evidence suggests considerable heating above the maximum temperature of greenschist stability (Fig. 13b). Therefore, preservation of prograde greenschist assemblages would require extensive and pervasive hydration reaction at low temperature followed by inhibition of the expected subsequent dehydration to amphibolite as the temperature increased.

These two points, together with the observation that the greenschist-facies assemblage is best developed in or near fractures, suggest instead that the greenschist assemblage in the distal parts of the aureole actually formed directly from the original amphibolite on the retrograde path, after the hydrothermal system had been established to provide the abundant H_2O required for reaction. Support for this hypothesis is provided by the absence of a precursor greenschist assemblage in the hornfelses developed close to the contact, consistent with a direct reaction of the original amphibolite assemblage to the pyroxene-bearing assemblage. Contact metamorphism in the mafic bands therefore involved prograde reaction of the amphibolite protolith to hornfels near the contact, with retrograde reaction of the protolith to greenschist far from the contact.

This model is very similar to that proposed for the basaltic country rocks on the eastern margin of the intrusion (Manning *et al.*, 1993). Manning *et al.* (1993) suggested that the availability of water was a critical factor controlling the development of metamorphic assemblages in the basalts. They suggested that the absence of an amphibolite assemblage intermediate to the greenschist and pyroxene hornfels zones was caused by the absence of suitable hydrous precursors in the basalts. The essentially unaltered and anhydrous precursor basalts did not react to greenschist on the prograde path, thus preventing the subsequent reaction to a hornblende-bearing assemblage; instead, the basalts reacted directly to the pyroxene facies. Manning *et al.* argued that the widespread greenschist-facies assemblage formed on the retrograde path, triggered by the onset of sufficiently vigorous hydrothermal circulation. We thus suggest that the timing of the development of the hydrothermal circulation system was similar in the basalts and the deeper, underlying gneisses.

Did water liberated from the metamorphosed gneisses infiltrate the intrusion?

The numerous pods, fracture-fillings and veins of pyroxene–plagioclase pegmatite in the Marginal Border Series

led Taylor & Forester (1979) and Irvine *et al.* (1998) to suggest that these features were a result of an influx of meteoric H_2O or metamorphic H_2O derived from the gneisses of the aureole. A super-solidus origin for these pegmatitic features seems likely, given their composition, mineral mode and stratigraphic dependence on crystallization pressure (Larsen & Tegner, 2006). This therefore suggests that any influx of H_2O required to form the pegmatites would necessarily have occurred during prograde metamorphism. The isotope systematics of both the intrusion itself and the gneiss on Kramer Island point to limited activity of the hydrothermal system in this region during contact metamorphism (Taylor & Forester, 1979), and the arguments presented above are consistent with a delayed onset of this limited hydrothermal circulation until the aureole was cooling down (and therefore the intrusion itself was mostly solidified). This suggests that significant quantities of meteoric H_2O did not enter the Marginal Border Series from the gneissic walls of the intrusion, although some may have been introduced to lower levels in the intrusion stratigraphy by the dehydration of altered blocks fallen from the roof (Taylor & Forester, 1979; Bindeman *et al.*, 2008; Wotzlaw *et al.*, 2012).

The H_2O budget in the Precambrian gneisses of the aureole was therefore a balance between the requirements of the H_2O-fluxed melting reactions in the quartzo-feldspathic gneiss and the supply of H_2O by amphibolite dehydration within ~150 m of the contact. Assuming the amphibolite contains 50 vol. % hornblende, containing 2 wt % H_2O, ~32 kg of H_2O can be liberated from each 1 m^3 of rock. Assuming the melt formed in the adjacent quartzo-feldspathic gneisses was fully H_2O-saturated and contained 6 wt % H_2O (at a pressure of ~0·2 GPa), 47 kg of H_2O per m^3 of gneiss would be required to produce an average melt fraction of 30%. Because the amphibolite bands form only a few volume per cent of the Precambrian gneiss in this part of Kramer Island, it is highly unlikely that the proximal amphibolite could have provided sufficient H_2O to flux the observed (assumed H_2O-saturated) melting in the immediately adjacent quartzo-feldspathic gneisses.

The result of this rudimentary calculation is consistent with petrographic evidence that there was insufficient H_2O to flux the expected amount of H_2O-saturated melt in the quartzo-feldspathic gneisses. Many gneisses close to the contact retain restitic quartz, plagioclase and K-feldspar despite Ti-in-quartz thermometry suggesting temperatures well in excess of the H_2O-present ternary minimum. Melting in these rocks was therefore most likely to have been inhibited by insufficient availability of H_2O. It is therefore equally unlikely that there would have been sufficient excess H_2O provided by devolatilization reactions in the aureole to account for the pegmatitic features described by Irvine *et al.* (1998).

In the distal parts of the aureole, the greenschist-facies veins, the almost complete replacement of original biotite and partial replacement of hornblende, and the highly turbid nature of the feldspars point to sufficient hydrothermal activity to trigger metamorphic reactions, although the oxygen isotope ratios are consistent with very low water/rock ratios (Taylor & Forester, 1979). No signs of meteoric water involvement are present in the proximal parts of the aureole, in which plagioclase, residual original biotite, and amphibole appear fresh and unaltered. This apparently pristine nature may be preserved because recrystallization and the healing of fractures and cracks during the prograde path reduced the permeability of the hottest parts of the aureole and inhibited pervasive flow of H_2O during the retrograde path.

CONCLUSIONS

The previously unstudied quartzo-feldspathic Precambrian gneisses forming the lower contact and floor of the Skaergaard intrusion provide a wealth of information about quartz recrystallization triggered by contact metamorphism, with subsequent H_2O-fluxed melting close to the contact. The profile of maximum temperature can be fitted with a simple thermal model, assuming realistic values for the thermodynamic and physical properties of the gneiss and the intrusion, and neglecting heat advection by hydrothermal circulation. Temperatures were generally much lower than those recorded in the basalts forming the upper walls and roof of the intrusion, supporting the suggestion of Norton & Taylor (1979) and Manning *et al.* (1993) that heterogeneous release of latent heat of crystallization played a role during fractionation and solidification. The availability of H_2O during metamorphism was critical in the development of the contact aureole in the gneiss. Melting close to the contact was apparently limited by the availability of H_2O on the prograde path, most probably because the limited hydrothermal circulation in the relatively impermeable and deeply buried gneiss did not begin until the peak temperatures were passed, and also because the minor amphibolite bands in the gneiss did not form a sufficiently large proportion of the total rock to supply enough H_2O by devolatilization reactions. This limited availability of H_2O during prograde reaction makes it most unlikely that either devolatilization or hydrothermal circulation in the aureole provided the source of H_2O required to form the pegmatites found in the margins of the intrusion.

Preliminary examination of the minor amphibolite bands suggests that the locally well-developed greenschist-facies replacement of the Precambrian amphibolites formed on the retrograde path, after the onset of limited hydrothermal circulation. Although the volumes of meteoric H_2O involved were insufficient to significantly alter the oxygen isotope ratios in the gneiss (Taylor & Forester, 1979) they

were sufficient for locally pervasive reaction to greenschist facies, although several hundreds of metres from the contact the greenschist facies is confined to veins and fractures.

ACKNOWLEDGEMENTS

This study formed the basis of N.A.B.'s MSc thesis at Cambridge University. Chris Richardson provided invaluable help and advice for the thermal modelling. We acknowledge helpful discussions with Dan McKenzie and Rune Larsen, as well as assistance with electron-probe microanalysis from Chiara Petrone and with cathodoluminescence from Stephen Reed. Helpful comments from Craig Manning, Alasdair Skelton and an anonymous reviewer greatly helped to improve the paper.

FUNDING

This work was supported by the Natural Environmental Research Council (NE/F020325/1). M.C.S.H. was supported by a Royal Society University Research Fellowship.

SUPPLEMENTARY DATA

Supplementary data for this paper are available at *Journal of Petrology* online.

REFERENCES

Ashley, K. T., Webb, L. E., Spear, F. S. & Thomas, J. B. (2013). *P–T–D* histories from quartz: A case study of the application of the TitaniQ thermobarometer to progressive fabric development in metapelites. *Geochemistry, Geophysics, Geosystems* **14**, 3821–3843.

Audétat, A. (2013). Origin of Ti-rich rims in quartz phenocrysts from the Upper Bandelier Tuff and the Tunnel Spring Tuff, southwestern USA. *Chemical Geology* **360–361**, 99–104.

Bindeman, I. N., Brooks, C. K., McBirney, A. R. & Taylor, H. P. (2008). The low-$\delta^{18}O$ late-stage ferrodiorite magmas in the Skaergaard Intrusion: result of liquid immiscibility, thermal metamorphism, or meteoric water incorporation into magma? *Journal of Geology* **116**, 571–586.

Bird, D. K., Brooks, C. K., Gannicott, R. A. & Turner, P. A. (1991). A gold-bearing horizon in the Skaergaard Intrusion, East Greenland. *Economic Geology* **86**, 1083–1092.

Cashman, K. V. (1993). Relationship between plagioclase crystallization and cooling rate in basaltic melts. *Contributions to Mineralogy and Petrology* **113**, 126–142.

Cook, S. J. & Bowman, J. R. (1994). Contact metamorphism surrounding the Alta stock; thermal constraints and evidence of advective heat transport from calcite + dolomite geothermometry. *American Mineralogist* **79**, 513–525.

Elmer, F. L., White, R. W. & Powell, R. (2006). Devolatilization of metabasic rocks during greenschist–amphibolite facies metamorphism. *Journal of Metamorphic Geology* **24**, 497–513.

Ferry, J. M. (1996). Three novel isograds in metamorphosed siliceous dolomites from the Ballachulish aureole, Scotland. *American Mineralogist* **81**, 485–494.

Ferry, J. M. (2001). Calcite inclusions in forsterite. *American Mineralogist* **86**, 773–779.

Ghiorso, M. S. & Gualda, G. A. R. (2013). A method for estimating the activity of titania in magmatic liquids from the compositions of coexisting rhombohedral and cubic iron–titanium oxides. *Contributions to Mineralogy and Petrology* **165**, 73–81.

Götze, J., Plötze, M. & Habermann, D. (2001). Origin, spectral characteristics and practical applications of the cathodoluminescence (CL) of quartz—a review. *Mineralogy and Petrology* **71**, 225–250.

Harris, N., McMillan, A., Holness, M., Uken, R., Watkeys, M., Rogers, N. & Fallick, A. (2003). Melt generation and fluid flow in the thermal aureole of the Bushveld Complex. *Journal of Petrology* **44**, 1031–1054.

Hayden, L. A. & Watson, E. B. (2007). Rutile saturation in hydrous siliceous melts and its bearing on Ti-thermometry of quartz and zircon. *Earth and Planetary Science Letters* **258**, 561–568.

Holland, T. & Powell, R. (2001). Calculation of phase relations involving haplogranitic melts using an internally consistent thermodynamic dataset. *Journal of Petrology* **42**, 673–683.

Holness, M. B. & Clemens, J. D. (1999). Partial melting of the Appin Quartzite driven by fracture-controlled H_2O infiltration in the aureole of the Ballachulish Igneous Complex, Scottish Highlands. *Contributions to Mineralogy and Petrology* **136**, 154–168.

Holness, M. B. & Isherwood, C. E. (2003). The aureole of the Rum Tertiary Igneous Complex, Scotland. *Journal of the Geological Society, London* **160**, 15–27.

Holness, M. B. & Sawyer, E. W. (2008). On the pseudomorphing of melt-filled pores during the crystallization of migmatites. *Journal of Petrology* **49**, 1343–1363.

Holness, M. B. & Watt, G. R. (2001). Quartz recrystallization and fluid flow during contact metamorphism: a cathodoluminescence study. *Geofluids* **1**, 215–228.

Holness, M. B. & Watt, G. R. (2002). The aureole of the Traigh Bhàn na Sgùrra Sill, Isle of Mull: reaction-driven micro-cracking during pyrometamorphism. *Journal of Petrology* **43**, 511–534.

Holness, M. B., Bickle, M. J. & Graham, C. M. (1991). On the kinetics of textural equilibration in forsterite marbles. *Contributions to Mineralogy and Petrology* **108**, 356–367.

Holness, M. B., Dane, K., Sides, R., Richardson, C. & Caddick, M. (2005). Melting and melt segregation in the aureole of the Glenmore Plug, Ardnamurchan. *Journal of Metamorphic Geology* **23**, 29–43.

Holness, M. B., Stripp, G., Humphreys, M. C. S., Veksler, I. V., Nielsen, T. F. D. & Tegner, C. (2011). Silicate liquid immiscibility within the crystal mush: late-stage magmatic microstructures in the Skaergaard Intrusion, East Greenland. *Journal of Petrology* **52**, 175–222.

Holness, M. B., Richardson, C. & Helz, R. T. (2012). Disequilibrium dihedral angles in dolerite sills: A new proxy for cooling rate. *Geology* **40**, 795–798.

Holtz, F., Behrens, H., Dingwell, D. B. & Taylor, R. P. (1992). Water solubility in aluminosilicate melts of haplogranite composition at 2 kbar. *Chemical Geology* **96**, 289–302.

Hoover, J. D. (1989). Petrology of the Marginal Border Series of the Skaergaard Intrusion. *Journal of Petrology* **30**, 399–439.

Huang, R. & Audétat, A. (2012). The titanium-in-quartz (TitaniQ) thermobarometer: A critical examination and re-calibration. *Geochimica et Cosmochimica Acta* **84**, 75–89.

Irvine, T. N., Andersen, J. C. Ø. & Brooks, C. K. (1998). Included blocks (and blocks within blocks) in the Skaergaard intrusion: Geologic relations and the origins of rhythmic modally graded layers. *Geological Society of America Bulletin* **110**, 1398–1447.

Jakobsen, J. K., Veksler, I. V., Tegner, C. & Brooks, C. K. (2005). Immiscible iron- and silica-rich melts in basalt petrogenesis documented in the Skaergaard intrusion. *Geology* **33**, 885–888.

Johannes, W. (1984). Beginning of melting in the granite system Qz–Or–Ab–An–H_2O. *Contributions to Mineralogy and Petrology* **86**, 264–273.

Kawasaki, T. & Osanai, Y. (2008). Empirical thermometer of TiO_2 in quartz for ultrahigh-temperature granulites of East Antarctica. In: Satish-Kumar, M., Motoyoshi, Y., Osanai, Y., Hiroi, Y. & Shiraishi, K. (eds) *Geodynamic Evolution of East Antarctica: a Key to the East–West Gondwana Connection. Geological Society, London, Special Publications* **308**, 419–430.

Kays, M. A., Goles, G. G. & Grover, T. W. (1989). Precambrian sequence bordering the Skaergaard Intrusion. *Journal of Petrology* **30**, 321–361.

Kularatne, K. & Audétat, A. (2014). Rutile solubility in hydrous rhyolite melts at 750–900°C and 2 kbar, with application to titanium-in-quartz (TitaniQ) thermobarometry. *Geochimica et Cosmochimica Acta* **125**, 196–209.

Landtwing, M. R. & Pettke, T. (2005). Relationships between SEM-cathodoluminescence response and trace-element composition of hydrothermal vein quartz. *American Mineralogist* **90**, 122–131.

Larsen, R. B. & Tegner, C. (2006). Pressure conditions for the solidification of the Skaergaard intrusion: eruption of East Greenland flood basalts in less than 300,000 years. *Lithos* **92**, 181–197.

Larsen, R. B., Jacamon, F. & Kronz, A. (2009). Trace element chemistry and textures of quartz during the magmatic hydrothermal transition of Oslo Rift granites. *Mineralogical Magazine* **73**, 691–707.

Leeman, W. P., MacRae, C. M., Wilson, N. C., Torpy, A., Lee, C.-T. A., Student, J. J, Thomas, J. B. & Vicenzi, E. P. (2012). A Study of Cathodoluminescence and Trace Element Compositional Zoning in Natural Quartz from Volcanic Rocks: Mapping Titanium Content in Quartz. *Microscopy and Microanalysis* **18**, 1322–1341.

Lind, A. (1996). Microstructural stability and the kinetics of textural evolutionPhD thesis, University of Leeds.

Liou, J. G., Kuniyoshi, S. & Ito, K. (1974). Experimental studies of the phase relations between greenschist and amphibolite in a basaltic system. *American Journal of Science* **274**, 613–632.

Manning, C. E. & Bird, D. K. (1991). Porosity evolution and fluid flow in the basalts of the Skaergaard magma–hydrothermal system, East Greenland. *American Journal of Science* **291**, 201–257.

Manning, C. E. & Bird, D. K. (1995). Porosity, permeability, and basalt metamorphism. In: Schiffman, P. & Day, H. W. (eds) *Low-Grade Metamorphism of Mafic Rocks: Geological Society of America Special Paper* **296**, p. 123–140.

Manning, C. E., Ingebritsen, S. E. & Bird, D. K. (1993). Missing mineral zones in contact metamorphosed basalts. *American Journal of Science* **293**, 894–938.

McBirney, A. R. (1989). The Skaergaard Layered Series: I. Structure and Average Compositions. *Journal of Petrology* **30**, 363–397.

McBirney, A. R., McBirney, C. & Imus, D. (1989). Geological map of the Skaergaard intrusion, east Greenland. University of Oregon.

McKenzie, D. (2011). Compaction and crystallization in magma chambers: towards a model of the Skaergaard Intrusion. *Journal of Petrology* **52**, 905–930.

Miyamoto, M. & Takeda, H. (1994). Thermal history of lodranites Yamato 74357 and MAC88177 as inferred from the chemical zoning of pyroxene and olivine. *Journal of Geophysical Research: Planets* **99**, 5669–5677.

Morgan, D. J., Jollands, M. C., Lloyd, G. E. & Banks, D. A. (2013). Using titanium-in-quartz geothermometry and geospeedometry to recover temperatures in the aureole of the Ballachulish Igneous Complex, NW Scotland. In: Llana-Fúnez, S., Marcos, A. & Bastida, F. (eds) *Deformation Structures and Processes within the Continental Crust. Geological Society, London, Special Publications* **394**, SP394.8.

Morgan, D. J., Jollands, M. C., Lloyd, G. E. & Banks, D. A. (2014). Using titanium-in-quartz geothermometry and geospeedometry to recover temperatures in the aureole of the Ballachulish Igneous Complex, NW Scotland. *Geological Society, London, Special Publications* **394**, 145–165.

Müller, A., Seltmann, R. & Behr, H.-J. (2000). Application of cathodoluminescence to magmatic quartz in a tin granite—case study from the Schellerhau Granite Complex, Eastern Erzgebirge, Germany. *Mineralium Deposita* **35**, 169–189.

Müller, A., Lennox, P. & Trzebski, R. (2002). Cathodoluminescence and micro-structural evidence for crystallisation and deformation processes of granites in the Eastern Lachlan Fold Belt (SE Australia). *Contributions to Mineralogy and Petrology* **143**, 510–524.

Müller, A., René, M., Behr, H.-J. & Kronz, A. (2003*a*). Trace elements and cathodoluminescence of igneous quartz in topaz granites from the Hub Stock (Slavkovský Les Mts., Czech Republic). *Mineralogy and Petrology* **79**, 167–191.

Müller, A., Wiedenbeck, M., Kerkhof, A. M. V. D., Kronz, A. & Simon, K. (2003*b*). Trace elements in quartz—a combined electron microprobe, secondary ion mass spectrometry, laser-ablation ICP-MS, and cathodoluminescence study. *European Journal of Mineralogy* **15**, 747–763.

Müller, A., Breiter, K., Seltmann, R. & Pécskay, Z. (2005). Quartz and feldspar zoning in the eastern Erzgebirge volcano-plutonic complex (Germany, Czech Republic): evidence of multiple magma mixing. *Lithos* **80**, 201–227.

Müller, T., Baumgartner, L. P., Foster, C. T. & Roselle, G. T. (2008). Forward modeling of the effects of mixed volatile reaction, volume diffusion, and formation of submicroscopic exsolution lamellae on calcite–dolomite thermometry. *American Mineralogist* **93**, 1245–1259.

Nielsen, T. F. D. (2004). The shape and volume of the Skaergaard Intrusion, Greenland: implications for mass balance and bulk composition. *Journal of Petrology* **45**, 507–530.

Norton, D. & Taylor, H. P. (1979). Quantitative simulation of the hydrothermal systems of crystallizing magmas on the basis of transport theory and oxygen isotope data: an analysis of the Skaergaard Intrusion. *Journal of Petrology* **20**, 421–486.

Ostapenko, G. T., Gamarnik, M. Y., Gorogotskaya, L. I., Kuznetsov, G. V., Tarashchan, A. N. & Timoshkova, L. P. (1987). Isomorphism of titanium substitution for silicon in quartz: experimental data. *Mineralogicheskii Zhurnal* **9**, 30–40.

Piazolo, S., Prior, D. J. & Holness, M. D. (2005). The use of combined cathodoluminescence and EBSD analysis: a case study investigating grain boundary migration mechanisms in quartz. *Journal of Microscopy* **217**, 152–161.

Platten, I. M. (1982). Partial melting of feldspathic quartzite around late Caledonian minor intrusions in Appin, Scotland. *Geological Magazine* **119**, 413–419.

Ramseyer, K. & Mullis, J. (1990). Factors influencing short-lived blue cathodoluminescence of alpha-quartz. *American Mineralogist* **75**, 791–800.

Ramseyer, K., Baumann, J., Matter, A. & Mullis, J. (1988). Cathodoluminescence colours of α-quartz. *Mineralogical Magazine* **52**, 669–677.

Rusk, B. G., Reed, M. H., Dilles, J. H. & Kent, A. J. R. (2006). Intensity of quartz cathodoluminescence and trace-element content in quartz from the porphyry copper deposit at Butte, Montana. *American Mineralogist* **91**, 1300–1312.

Rusk, B. G., Lowers, H. A. & Reed, M. H. (2008). Trace elements in hydrothermal quartz: Relationships to cathodoluminescent textures and insights into vein formation. *Geology* **36**, 547–550.

Salmonsen, L. P. & Tegner, C. (2013). Crystallization sequence of the Upper Border Series of the Skaergaard Intrusion: revised subdivision and implications for chamber-scale magma homogeneity. *Contributions to Mineralogy and Petrology* **165**, 1155–1171.

Schneider, C. A., Rasband, W. S. & Eliceiri, K. W. (2012). NIH Image to ImageJ: 25 years of image analysis. *Nature Methods* **9**, 671–675.

Seyedolali, A., Krinsley, D. H., Boggs, S., O'Hara, P. F., Dypvik, H. & Goles, G. G. (1997). Provenance interpretation of quartz by scanning electron microscope–cathodoluminescence fabric analysis. *Geology* **25**, 787–790.

Smith, J. V. & Brown, W. L. (1988). *Feldspar Minerals*. Springer.

Smith, J. V. & Stenstrom, R. C. (1965). Electron-excited luminescence as a petrologic tool. *Journal of Geology* **73**, 627–635.

Spear, F. S. & Wark, D. A. (2009). Cathodoluminescence imaging and titanium thermometry in metamorphic quartz. *Journal of Metamorphic Geology* **27**, 187–205.

Taylor, H. P. & Forester, R. W. (1979). An oxygen and hydrogen isotope study of the Skaergaard Intrusion and its country rocks: a description of a 55 M.Y. old fossil hydrothermal system. *Journal of Petrology* **20**, 355–419.

Tegner, C., Thy, P., Holness, M. B., Jakobsen, J. K. & Lesher, C. E. (2009). Differentiation and compaction in the Skaergaard Intrusion. *Journal of Petrology* **50**, 813–840.

Thomas, J. B. & Watson, E. B. (2012). Application of the Ti-in-quartz thermobarometer to rutile-free systems. Reply to: a comment on: 'TitaniQ under pressure: the effect of pressure and temperature on the solubility of Ti in quartz' by Thomas *et al*. *Contributions to Mineralogy and Petrology* **164**, 369–374.

Thomas, J. B., Bruce Watson, E., Spear, F., Shemella, P., Nayak, S. & Lanzirotti, A. (2010). TitaniQ under pressure: the effect of pressure and temperature on the solubility of Ti in quartz. *Contributions to Mineralogy and Petrology* **160**, 743–759.

Thy, P., Lesher, C. E., Nielsen, T. F. D. & Brooks, C. K. (2006). Experimental constraints on the Skaergaard liquid line of descent. *Lithos* **92**, 154–180.

Tuttle, O. F. & Bowen, N. L. (1958). *Origin of Granite in the Light of Experimental Studies in the System $NaAlSi_3O_8$–$KAlSi_3O_8$–SiO_2–H_2O. Geological Society of America, Memoirs* **74**, 146 p.

Vernon, R. H. (2004). *A Practical Guide to Rock Microstructure*. Cambridge University Press.

Wager, L. R. & Brown, G. M. (1968). *Layered Igneous Rocks*. W. H. Freeman.

Wager, L. R. & Deer, W. A. (1939). *Geological Investigations in East Greenland, Part III. The Petrology of the Skaergaard Intrusion, Kangerdlugssuaq, East Greenland. Meddelelser om Gronland* **105**, 352 p.

Wark, D. A. & Watson, E. B. (2006). TitaniQ: a titanium-in-quartz geothermometer. *Contributions to Mineralogy and Petrology* **152**, 743–754.

Watt, G. R., Oliver, N. H. S. & Griffin, B. J. (2000). Evidence for reaction-induced microfracturing in granulite facies migmatites. *Geology* **28**, 327–330.

Wilson, C. J. N., Seward, T. M., Allan, A. S. R., Charlier, B. L. A. & Bello, L. (2012). A comment on: 'TitaniQ under pressure: the effect of pressure and temperature on the solubility of Ti in quartz', by Jay B. Thomas, E. Bruce Watson, Frank S. Spear, Philip T. Shemella, Saroj K. Nayak and Antonio Lanzirotti. *Contributions to Mineralogy and Petrology* **164**, 359–368.

Wotzlaw, J.-F., Bindeman, I. N., Schaltegger, U., Brooks, C. K. & Naslund, H. R. (2012). High-resolution insights into episodes of crystallization, hydrothermal alteration and remelting in the Skaergaard intrusive complex. *Earth and Planetary Science Letters* **355**, 199–212.